Classification of igneous rocks analyzed by ChemCam at Gale crater, Mars

Agnès Cousin, Violaine Sautter, Valérie Payré, Olivier Forni, Nicolas Mangold, Olivier Gasnault, Laetitia Le Deit, Jeff Johnson, Sylvestre Maurice, Mark Salvatore, et al.

LA-UR-17-27692 (Accepted Manuscript)

Classification of igneous rocks analyzed by ChemCam at Gale crater, Mars

Cousin, Agnes; Sautter, Violaine; Payre, Valerie; Forni, Olivier; Mangold, Nicolas; Gasnault, Olivier; Le Deit, Laetitia; Johnson, Jeff; Maurice, Sylvestre; Salvatore, Mark; Wiens, Roger Craig; Gasda, Patrick J.; Rapin, William

To be published in: Icarus

DOI to publisher's version: 10.1016/j.icarus.2017.01.014

Permalink to record: http://permalink.lanl.gov/object/view?what=info:lanl-repo/lareport/LA-UR-17-27692

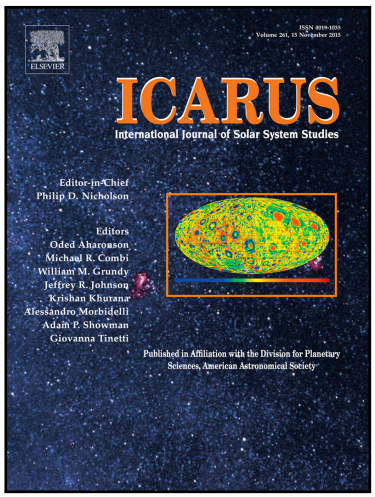

Classification of Igneous Rocks analyzed by ChemCam at Gale Crater, Mars.

Violaine Sautter , Valérie Payré , Olivier Forni , Nicolas Mangold , Olivier Gasnault , Laetitia Le Deit , Jeff Johnson , Sylvestre Maurice , Mark Salvatore , Roger C Wiens , Patrick Gasda , William Rapin , Agnes Cousin

PII: S0019-1035(16)30457-2
DOI: 10.1016/j.icarus.2017.01.014
Reference: YICAR 12336

To appear in: *Icarus*

Received date: 3 August 2016
Revised date: 5 January 2017
Accepted date: 17 January 2017

Please cite this article as: Violaine Sautter , Valérie Payré , Olivier Forni , Nicolas Mangold , Olivier Gasnault , Laetitia Le Deit , Jeff Johnson , Sylvestre Maurice , Mark Salvatore , Roger C Wiens , Patrick Gasda , William Rapin , Agnes Cousin , Classification of Igneous Rocks analyzed by ChemCam at Gale Crater, Mars., *Icarus* (2017), doi: 10.1016/j.icarus.2017.01.014

Highlight

- ChemCam onboard Curiosity at Gale crater, Mars, has analyzed 59 igneous rocks during the first 800 sols.
- Igneous rocks encountered at Gale crater show different textures: aphanitic, coarse and fine-grained, and even porphyritic.
- Feldspar-rich rocks are observed mainly close to the Peace Vallis alluvial fan.
- Mafic minerals correspond to Fe-rich pigeonites and Fe-rich augites, as observed in some mars meteorites such as NWA 7034.
- Some of the basalts encountered at Gale show a low Mg# and are therefore different from the basalts observed by the MER.

Classification of Igneous Rocks analyzed by ChemCam at Gale Crater, Mars.

Corresponding author: Agnes Cousin (agnes.cousin@irap.omp<mailto:agnes.cousin@irap.omp>.
Co-authors:
Violaine Sautter[b], Valérie Payré[c], Olivier Forni[a], Nicolas Mangold[d], Olivier Gasnault[a], Laetitia Le Deit[d], Jeff Johnson[e], Sylvestre Maurice[a], Mark Salvatore[f], Roger C Wiensg, Patrick Gasdag, William Rapina.
a: Institut de Recherche en Astrophysique et Planétologie, IRAP, 31028 Toulouse, France
b: Institut de Minéralogie, de Physique des Matériaux et de Cosmochimie, IMPMC, 75005 Paris, France
c: Université de Lorraine, 54000 Nancy, France
d: Laboratoire de Planétologie et Géophysique de Nantes, Université de Nantes, 44300 Nantes, France
e: Johns Hopkins University Applied Physics Laboratory, 11101 Johns Hopkins Road 200-W230 Laurel, MD 20723-6005
f: University of Michigan-Dearborn, 4901 Evergreen Road, Dearborn, MI 48128, US
g: Los Alamos National Laboratory, LANL, Los Alamos 87545, NM, US

Abstract

Several recent studies have revealed that Mars is not a simple basalt-covered planet, but has a more complex geological history. In Gale crater on Mars, the Curiosity rover discovered 59 igneous rocks. This paper focuses on their textures (acquired from the cameras such as MAHLI and MastCam) and their geochemical compositions that have been obtained using the ChemCam instrument. Light-toned crystals have been observed in most of the rocks. They correspond to feldspars ranging from andesines/oligoclases to anorthoclases and sanidines in the leucocratic vesiculated rocks. Darker crystals observed in all igneous rocks (except the leucocratic vesiculated ones) were analyzed by LIBS and mainly identified as Fe-rich pigeonites and Fe-augites. Iron oxides have been observed in all groups whereas F-bearing minerals have been detected only in few of them. From their textural analysis and their whole-rock compositions, all these 59 igneous rocks have been classified in five different groups; from primitive rocks i.e. dark aphanitic basalts/basanites, trachybasalts, tephrites and fine/coarse-grained gabbros/norites to more evolved materials i.e. porphyritic trachyandesites, leucocratic trachytes and quartz-diorites. The basalts and gabbros are found all along the traverse of the rover, whereas the felsic rocks are located before the Kimberley formation, i.e. close to the Peace Vallis alluvial fan deposits. This suggests that these alkali rocks have been transported by fluvial activity and could come from the Northern rim of the crater, and may correspond to deeper strata buried under basaltic regolith (Sautter et al., 2015). Some of the basaltic igneous rocks are surprisingly enriched in iron, presenting low Mg# similar to the nakhlite parental melt that cannot be produced by direct melting of the Dreibus and Wanke (1986) martian primitive mantle. The basaltic rocks at Gale

are thus different from Gusev basalts. They could originate from different mantle reservoirs, or they could have undergone a more extensive fractional crystallization. Gale basaltic rocks could have been the parental magma of residual liquid extending into alkali field towards trachyte composition as magma fractionated under anhydrous condition on its way to the surface before sub adiabatic ascent.

I. Introduction

The chemistry and mineralogy of the Martian surface are increasingly well constrained thanks to a combination of orbital spectroscopy (e.g. Mars Odyssey, Mars Reconnaissance Orbiter, Mars Express), study of the Martian meteorites and *in situ* analyses (landers and rovers such as Pathfinder, Spirit, Opportunity, Phoenix and Curiosity). All of these lines of evidence point to a primary magmatic crust that is globally basaltic (McSween et al., 2003 and 2009). However, this vision is evolving based on recent observations. In particular, rocks of the ancient Noachian period appear to include a variety of felsic igneous rocks. From orbit, the combination of TES and THEMIS data indicated the rare occurrence of quartzo-feldspathic material excavated from depth (Bandfield et al., 2004; Bandfield, 2006). More recently, the improved spatial resolution of the Compact Reconnaissance Imaging Spectrometer for Mars (CRISM) visible/near-infrared (VNIR) spectrometer (< 20 m per pixel) has led to the identification of several localities that are particularly rich in anorthosite in the southern highlands (Carter and Poulet, 2013; Wray et al., 2013). The recently discovered Martian regolith breccia 7034 and paired samples document for the first time magmatic diversity during the Noachian period, as they contain highly differentiated felsic clasts, orthopyroxene-dominated mafic lithologies, strong evidence for impacts (melt spherule, vitrophyres), lithic and mineral clasts of all sizes including 4.43 Ga old zircons (Agee et al., 2013; Humayun et al., 2014; Nyquist et al., 2016). This meteorite may be the first representative sampling of the Noachian Martian crust.

The Mars Science Laboratory (MSL) rover Curiosity, which landed in Gale crater in 2012 at the northern edge of the heavily cratered Noachian highlands, discovered evidence supporting such a magmatic diversity (Stolper et al., 2013; Sautter et al., 2014, 2015, 2016; Schmidt et al., 2014). These observations of igneous targets are of great interest as they provide a unique window into the planetary interior (mantle partial melt, magma fractionation or crystal accumulation). Curiosity's drive began at Bradbury Landing, on a plain at a distal portion of the alluvial fan derived from Peace Vallis, a fluvial channel cutting through the northern rim of Gale crater. The rover crossed these hummocky plains during the first 60 sols (Martian days). Then, the rover entered into a region named Yellowknife Bay where exposed sedimentary rocks, namely mudstones and sandstones, were interpreted as fluvial and lacustrine deposits (Grotzinger et al., 2014; McLennan et al., 2014). After leaving Yellowknife Bay, the rover started the traverse to the main mission objective, the basal layers of Aeolis Mons, colloquially referred to as Mt. Sharp (as will be used throughout this manuscript) that were reached at Pahrump Hills, on sol 750 (Grotzinger et al., 2015). Overall, in 4 years, the rover has driven > 13 km; during the first 800 sols it characterized ~150 rocks with distinct igneous and sedimentary textures (Sautter et al., 2014, 2015; Schmidt et al., 2014; Mangold et al., 2016b).

The Curiosity rover has the ability to characterize rock textures and compositions at a variety of distances with its sophisticated payload. Two remote instruments are located on the top of the rover mast. The MastCam instrument (Malin et al., 2010; Bell et al., 2012) is a set of 2 cameras mounted on the rover mast that provides critical contextual images. ChemCam is a Laser Induced Breakdown Spectrometer (LIBS) combined with a high-resolution imager (Remote Micro Imager "RMI" - Wiens et al., 2012; Maurice et al., 2012). Two complementary instruments that constrain mineralogy and chemistry are also onboard: CheMin, an X-ray diffractometer (Blake et al., 2012); the arm-mounted Alpha Particle X-Ray Spectrometer (APXS) providing contact analyzes of rocks and soils over a ~1.7 cm in diameter surface (Campbell et al., 2012).

Among these instruments, only Mastcam and ChemCam were used for extensive characterization of igneous rocks. Most of these targets were analyzed by opportunistic science, i.e., analyses were made during the traverse without stopping the rover for contact science or drilling, both of which require deployment of the ~200 kg rover arm. The drill (and hence also CheMin) has not been used on igneous rocks because organics – a major goal of Curiosity - are not expected to be stored easily in such rocks, and also these igneous rocks present other challenges: they are generally float rather than bedrocks (may tend to move when being drilled) and relatively hard (leading to more rapid drill bit wear).

The objective of this study is to classify and review the wide range of igneous rocks observed during the traverse to Mt Sharp from sol 20 to sol 800 (Figure 1) using the ChemCam instrument. This instrument gives access to the chemistry of rocks and soils at the sub-millimeter scale and is widely used on Mars due to its tactical ease, as targets can be analyzed up to 7 m away from the rover. On average more than two targets are sampled every operational day. Therefore, ChemCam has, by far, analyzed a much larger number of samples than any instrument onboard the rover, with more than 1000 sampled Martian targets, corresponding to >300000 individual spectra, >6000 images, and many passive spectra providing a unique statistical sampling along the rover traverse (Maurice et al., 2016).

In the present paper, we first describe the textures of the igneous targets using the large number of images acquired by the rover, as a means of differentiating intrusive from extrusive rocks. Next, when possible, sub-millimeter scale chemical analyses are superposed with RMI images to characterize the chemistry and then infer the mineralogy of these samples. In tandem, these textural and chemical analyses are used for a petrological assessment of the selected rocks. Finally, the geographical and statistical distributions of the different rock types are discussed on the scale of the crater as a whole.

II. Methodology

The primary classification of igneous rocks should be based on mineral size and modal distribution. Volcanic rocks range from aphanitic to phaneritic textures. For aphanitic rocks including glass or when crystals are smaller than the lower limit of grain detection of the Curiosity remote cameras (~0.3 mm - Mangold et al. 2016b), textural characterization requires additional qualitative observations. Glassy textures are identified by their shiny surface, vesicular and conchoidal appearance. On phaneritic rocks (grain size > 0.3mm) preliminary mineral estimates are done based on shape and color, allowing at least the discrimination of felsic phases from mafic ones. This allows an evaluation of their respective modal proportions. Then, point-by-point measurements of elemental chemistry at sub-millimeter spatial scales are analyzed using

multivariate techniques (Wiens at al., 2013; Clegg et al., 2016) that allow classification of spectra from a mineral perspective. Finally, whole rock composition is estimated for targets with sufficient sampling (i-e large 2-D rasters, at least 9 observation points). For fine-grained rocks that show equigranular textures (typically where grain size is smaller than the beam size), whole rock composition is obtained by averaging all of the individual analyses on that sample. When rocks are heterogeneous, such as when they exhibit phenocrysts in a cryptocrystalline matrix, we combine modal proportion with average compositions obtained on both felsic and mafic points (Sautter et al., 2015).

Images

The three cameras onboard Curiosity used in this study are MastCam, MAHLI, and ChemCam RMI. Each has its own unique yet complementary imaging capabilities (Table 1).

MastCam (Malin et al., 2010; Bell et al., 2012) is a combination of two cameras, located on top of the mast just below the ChemCam instrument. Their main objective is to acquire multispectral images and panoramas to provide geologic context. Given their imaging capabilities, they can distinguish grains with sizes larger than 500 µm at 3 m distance. Mastcam is widely used and is of particular interest to study the morphology and texture of rocks.

MAHLI ("Mars Hand Lens Imager") is a high-resolution camera located on the arm of the rover. It has the capability to focus from 2.1 cm up to infinity, which gives the opportunity to access the textures of rocks in detail (it can distinguish grains as small as 45 µm in size at 2 cm distance; Edgett et al., 2013). Unfortunately, this camera cannot be used at its greatest spatial resolution for each target that is sampled by ChemCam, as its mobility is constrained by its position on the arm. Therefore, MAHLI images of rocks investigated in this paper are quite rare, or have already been discussed in previous papers.

RMI ("Remote Micro Imager") is part of the ChemCam instrument. It is a black and white camera able to distinguish grains as small as 80 µm (at 2 m distance) or 120 µm (at 3 m distance) (Langevin et al., 2013; Le Mouélic et al., 2015). RMI field of view is 20 mrad. It is used both before and after ChemCam LIBS analyses on each target in order to give a detailed context of each point analysis. The resulting data allow for careful description of the rocks, including dust cover, compaction etc.

Elemental composition

Chemical analyses used in the present study have been obtained exclusively from the ChemCam instrument, which is the most used thanks to its remote sensing technique. This instrument is located on top of the mast of the rover and uses the LIBS technique (Laser Induced Breakdown Spectroscopy), which focuses a laser on a target to create plasma containing the elemental species present in this target. The analysis of the plasma light by spectroscopy yields the chemical composition of the rock. Targets can be sampled without preparation and at distances up to 7 m from the instrument.

The small, 350-550 µm footprint of the analysis (Maurice et al., 2012) cannot be increased in size to generate bulk rock compositions, as a high laser power density is needed to create a plasma. Instead, multiple observation points can be used on each target and aggregated to estimate bulk compositions. Standard observations include 5 observation points up to 25 observation points on each target either collected in lines or in grid patterns. Each observation point typically corresponds to 30 laser shots (i.e., 30 spectra) with each shot coring slightly deeper into the sample, allowing for the possibility to investigate compositional variability with depth. ChemCam's sub-millimeter footprint provides a great opportunity to access the

composition of individual crystals in a rock, as point-to-point variations in chemistry often reflect variations in individual grains.

The chemical heterogeneity of a given rock target can be assessed by using a statistical tool called the "Gini index" (Gini, 1921; Eliazar et al., 2010). This index is calculated using the dispersion around the average value. At least 9 observation points in the same target have to be available in order to perform this calculation. The Gini index ranges from 0 to 1: the smaller it is, the more homogeneous the target is, and vice-versa. Mangold et al (2016b) have validated this index by comparing it to the actual grain size deduced from MAHLI image analyses. They are quite well correlated: homogeneous chemistry and small grain size (less than 300 μm) give G < 0.25; chemical heterogeneity observed for G between 0.25 and 0.5 corresponds to grain sizes close to and slightly larger than the laser beam size (between 250 μm and 1 mm); heterogeneous chemistry is observed for G > 0.5 and correspond to grain sizes larger than 1 mm. Such a parameter should be used cautiously, as rocks with coarse grains of similar composition (e.g., a coarse-grained monomineralic rock in the extreme case) would not show high variability.

Major element compositions

In order to quantify the major element abundances (SiO_2, TiO_2, Al_2O_3, FeO_T, MgO, CaO, Na_2O, and K_2O) the ChemCam team is using a combination of two multivariate techniques: the "Partial Least Squares" (PLS) and the "Independent Component Analysis" (ICA). Recalibration was completed in 2015, expanding the standard database from 65 to 450 standards enabling a better determination of major elements (Wiens et al., 2015; Clegg et al., 2016). The PLS method uses different emission lines of a given element and compares them to known standards analyzed in a test bed on Earth (Clegg et al. 2009, Wiens et al. 2013). This technique has been updated by using sub-models depending on the range of compositions for each element (Anderson et al., 2016). The ICA technique used to classify ChemCam data (Forni et al., 2009, 2013; Lasue et al., 2011) is derived from blind source separation research (Hyvärinen et al., 2001) and identifies different statistically independent components and allowing spectra to be sorted from these components. Regression laws have been performed for each element, between the ICA score and the known-compositions of the reference spectra.

The accuracy of ChemCam predictions is estimated by calculating the root mean squared error of prediction (RMSEP) for a representative test set of geostandards for each major element. This RMSEP varies as a function of elemental abundance, and is calculated by creating a look-up table using a test-set. The precision of ChemCam is determined from the standard deviations of multiple observations of homogeneous targets. The Yellowknife Bay mudstone (Mangold et al., 2015) provides an upper limit for the precision, allowing for some slight variation in the mudstone compositions. These are generally consistent with precision determined from observations of the onboard calibration targets, which yielded precisions for SiO_2 (1.5 wt.%), TiO_2 (0.14 wt.%), Al_2O_3 (0.57 wt.%), FeO_T (1.8 wt.%), MgO (0.49 wt.%), CaO (0.42 wt.%), Na_2O (0.49 wt.%), and K_2O (0.14 wt.%) (Blaney et al., 2014). It should be noted that published errors for APXS typically only represent precision and not accuracy. The precisions obtained by ChemCam are just slightly higher than those of the APXS. For more details on accuracy and precision of ChemCam data, see Clegg et al. (2016).

Minor and trace-element compositions

Minor and trace elements such as Mn, Sr, Li, Ba, Rb and F have been quantified using a univariate. This quantification has been developed on the new database using more than 400 samples for specific elements such as Ba, Sr and Rb (Payré et al., 2016). Mn has been quantified using the regression law defined from a dedicated suite of samples by Lanza et al (2016). A dedicated suite of twelve mixtures of F-bearing materials was used to quantify F abundance through the development of a univariate regression law (Forni et al., 2015).

III. Textural Analysis

Images from MastCam, RMI and MAHLI have been used to determine the context of the targets, their morphology and texture. Throughout Gale crater, hard rocks occur either as float or as discontinuous outcrops. Distinguishing igneous rocks from sedimentary rocks is particularly difficult for rocks with grain sizes less than 100 μm where textures and chemical variations related to individual grains become impossible to untangle. In order to differentiate lavas from fine-grained sandstones or pyroclastic flows, other morphological criteria are used such as scoriaceous or vesicular surface features and conchoidal fracturing. Stratified outcrops that show layering with local cross-bedding features are potentially observed in volcanoclastic sediments such as distal tephra deposits (Manville et al., 2009). The present study focuses solely on effusive and intrusive igneous rocks, excluding any putative volcanoclastic rocks. Therefore, samples with layered structure cross-stratification or any kind of sedimentary features such as pebbles were discarded, in agreement with their predominant interpretation as fluvial and lacustrine origin (Grotzinger et al., 2014, 2015), with exception of individual pebble analyses. Also, rocks with undefined textures (Mangold et al., 2016b) such as Jake_M (Stolper at al., 2013) have been eliminated for this study. More details on rock classification can be found in Mangold et al., 2016b.

Igneous rocks encountered along the traverse to sol 800 have been observed as clasts in conglomerates or float rocks lying on soils or partly buried in them. They are heterogeneous in texture, grade in color from dark grey to light-toned and often present facets due to wind erosion (ventifacts). The morphology and texture of igneous rocks, which vary significantly due to variations in grain size, allow for the distinction between effusive and intrusive rocks.

Targets considered as igneous rocks are listed in Table 2, with the sol number when they were analyzed and the number of ChemCam observation points for each target. We were able to characterize 59 hard targets totalizing 419 observation points consisting of more than 12,500 individual LIBS spectra.

III. 1. Effusive rocks

Effusive rocks can be classified in three different groups depending on their color, morphology and texture:

Group 1 (20 rocks - Figure 2a,b) corresponds to dark-toned rocks, with an aphanitic texture, i.e. relatively fine-grained (< 0.3 mm) rocks in which most of the individual crystals cannot be distinguished on RMI images. Most of these rocks contain some light-toned microliths that are predominantly smaller than the laser beam (~ 350 μm) although locally up to 2.5 mm in length for microliths in Aztec and Warm_Spring. Dark-toned crystals such as olivine phenocrysts described in Adirondack-class basalts from Gusev crater and analyzed by the Spirit rover (McSween et al. 2003, 2006a, 2006b) have not been observed in these dark rocks at Gale. Some

of these rocks are shiny with no visible grains and exhibiting local conchoidal fractures, which is typical of glassy or extremely fine-grained material. One rock (Laurens) shows a scoriaceous/vesicular texture. These rocks have been encountered as float rocks and increase in number after sol 400.

Group 2 (10 rocks – Figure 2c,d) consists of porphyritic rocks with large light-toned euhedral phenocrysts set in a dark grey fine-grained mesostasis with no resolved individual grains. Where possible given image quality, a detailed modal analysis was performed to obtain the proportion of the phenocrysts in the whole rock. Modal abundances based on the RMI images were analyzed with ImageJ software. The RMI image was first converted to a binary image in which feldspar crystals appear in white and dark crystals in black. Areas of the image were then analyzed to determine the percentage of leucocratic material. Such estimates have been performed on four rocks: Horlick, Robin_Hood, Harrison and Bindi. In Horlick, Robin_Hood and Harrison, the phenocrysts represent between 45 and 57% of the rock, whereas Bindi appears to be a cumulate with the phenocrysts representing around 80% of the rock. Harrison contains the biggest phenocrysts, up to 20 mm in length and between 1 and 3 mm width. The other porphyritic rocks contain phenocrysts around 2 mm in size. Some of the float rocks of this group have been identified as trachyandesites by Sautter et al. (2015). These rocks have been seen as float rocks or clasts in conglomerates (such as Harrison). The sub-rounded morphology of some of them suggests that they could be ancient clasts in conglomerates that are now disaggregated (Sautter et al. 2016).

Group 3 (6 rocks - Figure 2e,f) contains light-toned rocks (called “leucocratic rocks” throughout the manuscript) with almost no visible grains (some of them such as Stark contain a few light-toned microliths), sometimes showing conchoidal fractures and having a vesiculated or pumiceous appearance. Some of the rocks of this group have been identified as trachytes by Sautter et al. (2015). All of these rocks have been encountered as float, but also in some cases forming slabs covered by dust (Sledgers). Vesicles are rounded in shape (Blanchet, Stark and Becraft) or stretched forming flutes showing evidence for magmatic flow (Meeting_House).

III.2. Intrusive rocks

Two groups of intrusive rocks have been identified based largely on color and grain size.

Group 4 (10 rocks – Figure 3a,b) comprises dark rocks that are either fine-grained (< 1mm but still larger than the laser beam: Beacon, Coronation) or coarse-grained (up to 3 mm: La Reine, Black_Trout, Mara) with the same proportion of dark and light euhedral crystals. This equigranular texture and the ratio close to 1 between mafic and felsic crystals are typical of intrusive rocks. These rocks in Group 4 are always observed as floats and have largely rounded edges with flat or curved facets.

Group 5 (13 rocks - Figure 3c,d) includes leucocratic coarse intrusive (> 5mm) rocks. Light-toned anhedral crystals represent up to 80% of the rock. Some of these rocks show rectangular translucent grey grains (~ 1mm) intergrown within coarse, pearly pink crystals (e.g. Clinton target). Secondary minerals gathered within dark material correspond to ~20% of the rock. These rocks are either pristine and sometimes in contact with darker fine-grained rocks (Nita) or fragmented and weathered (Angmaat, Bird_River, Little_Wind _River, Wikinson, Kodak and Dougalls). Some of these rocks were characterized as quartz-diorites/granodiorites by Sautter et al. (2015). They occur mainly as float but some have unknown settings because they are partially buried (Ross). These rocks were exclusively encountered near the landing site (before sol 550).

IV. Chemistry

ChemCam is the first "microprobe" sent to Mars with the potential to analyze individual minerals at rock-forming scales (Wiens et al., 2015). However, the laser beam size (300-500 μm – Maurice et al., 2012) is such that mineral mixtures are still often analyzed rather than individual crystals, especially for fine-grained rocks where grain size is less than or comparable to the beam size.

We have combined visual observations detailed in part III with the Gini index for all the possible targets (those with at least 9 observation points) for each group. The average index obtained for aphanitic dark rocks (Group 1) is relatively low, around 0.52, whereas for fine-grained rocks (Group 4) it is slightly higher (0.56). It is even more elevated, between 0.8 and 0.76, for coarse-grained and porphyritic rocks (Group 5 and Group 2, respectively). The average Gini index for rocks of Group 3 is similar to the one of Group 1 (0.53), but this has been calculated from only 2 rocks (as only 2 rocks have been sampled with at least 9 observation points). The results from the Gini index are consistent with our visual observations, aphanitic rocks being relatively homogeneous whereas crystallized rocks are heterogeneous at the scale of LIBS analyses.

Due to the small scale of the ChemCam analyses, we must combine the chemical data with the interpretation of the RMI images where feldspar minerals are easily observed (euhedral late-shaped whitish crystals) compared to mafic phases, before inferring any mineral composition from such analyses. Therefore this chemistry section is focusing on chemical diagrams that are useful to decipher between several mineralogical phases. Such diagrams showing shot to shot variations in composition with depth (25 spectra per observation point, the first 5 points being removed to avoid dust contamination) are used in a complementary way to display both mafic and felsic phases (e.g., plots of FeO_T versus SiO_2, lacking Mossbauer instrument on Curiosity, all iron is taken as Fe^{2+}) and to differentiate between feldspars (Al_2O_3 versus $Na_2O + K_2O$). Figure 4 displays the results obtained for one representative rock of each group.

As suggested in the textural description above, aphanitic dark rocks (Group 1) do not show any crystals with the exception of a few occasional light-toned microliths that are generally smaller than the beam size. From RMI images and chemical diagrams such as Figure 4a-b, a limited number of LIBS points have sampled a combination of these microliths and the surrounding matrix (Points #6, #8 and #10). The corresponding chemical compositions are the most alkali, aluminum-rich of these rocks, providing evidence of some felsic phase (Figure 4a-b, # 6). Nevertheless, all the points plot close to each other as a cluster, which shows that these types of targets are homogeneous, as observed with the images and quantified by the Gini index in the previous paragraph.

Group 2 targets, with their porphyritic texture, include a large amount of elongated light-toned minerals (see part III.1 and figure 2c, d) with a grain size larger than the beam size. Therefore, ChemCam was able to sample relatively clean light-toned crystals (without or with very low contributions from the mafic matrix, i.e. $FeO_T < 10\%$). For example, in the sample Harrison, leucocratic phenocrysts clearly stand out chemically from the mafic component (Figure 4c) and the zoning typically seen in elongated light-toned minerals (Sautter et al., 2016) is easily

observed; the laser sampled light grey cores (Figure 4d points # 12, 14, 15, and 16, with SiO_2 50-55% and Al_2O_3 > 20%) and whitish rims (points # 3 and # 8, SiO_2 ~60% and Al_2O_3 ~19%). Point #5 is especially enriched in FeO_T (> 40 wt.%) and low in SiO_2 (<30 wt.%).

In Figure 4e-f, all but one point of the Group 3 rocks correspond to a light-toned phase that is K-feldspar-rich (SiO_2> 65% and $Na_2O + K_2O$ around 12%). The unique point, #3, contains ~ 13% FeO_T and a smaller amount of SiO_2 (< 60%). It seems to be a mixture between an oxide and a felsic-rich matrix, which is consistent with visual analyses.

In intrusive fine-grained rocks (Group 4), small light-toned crystals and dark crystals are distinguished from each other both texturally and chemically (negative FeO_T vs SiO_2 trends and positive Al_2O_3 vs $Na_2O + K_2O$ trends, respectively, in Figure 4g-h). Point #6 from Ashuanipi exemplifies a rather clean plagioclase composition whereas points #4, #8 and #9 present a more mafic trend, with point #2 particularly low in SiO_2, Al_2O_3 and alkali.

For intrusive targets of Group 5 (Figure 4i-j), 80% of the points display higher silica than the mean martian crust derived from soil composition (SiO_2 50-65%) (Taylor and McLennan et al., 2009), combined with low Fe abundance (FeO_T < 10%), and relatively high aluminum (Al_2O_3 > 20%) and calcium (CaO~10%) abundances, thus suggesting rocks dominated by plagioclase phases.

These chemical trends are useful for such small-scale analyses as performed by ChemCam in order to chemically decipher between mafic and felsic phases. This is complementary to the visual observations, and a necessary first step before inferring the mineralogy of the sampled targets. From this part we can conclude that Group 1 corresponds to mafic-dominated rocks whereas Group 2, Group 3 & Group 5 are felsic-dominated rocks, while Group 4 is intermediate.

V. Mineralogy

Assessing the mineralogy of the sampled targets is then possible using the ChemCam data by combining the visual and chemical observations. If a white rectangular-shaped crystal is Fe-Mg-poor, then a feldspar crystal is likely to have been probed and projection in an Ab-An-Or triangle becomes possible. Mafic compositions are trickier, as it is difficult to distinguish pyroxenes, oxide phases, olivine and amphiboles in the RMI images within the dark portions of rocks. However, Figure 4 showed that we can still easily texturally distinguish the mafic phases based on the chemical data.

1-Feldspar phases

As suggested in the textural description, aphanitic dark rocks (Group 1) do not show any crystals, with the exception of a few occasional light-toned microliths that are generally smaller than the beam size. However, as shown in Figure 4a-b, these rocks are really homogeneous, with a mafic composition even for points that may have sampled a microlith (see part IV). Therefore no points from Group 1 can be plotted on a feldspar ternary diagram (Or-Ab-An).

All of the selected LIBS points that sampled a light-toned phase for all the other groups of rocks have been plotted in a ternary diagram (Figure 5). For clarity, points from dark-toned (Groups 2 and 4) and light-toned rocks (Groups 3 and 5) are shown in two distinct diagrams.

Plagioclases observed in dark-toned rocks correspond to andesine (Figure 5a) with only a few exceptions, mainly in the Harrison target where phenocryst rim compositions plot closer to

the alkali end-member due to the zoning mentioned above (Figure 5b). Several points from the intrusive rocks of Group 4 plot at the interface with the immiscibility gap (Figure 5a). This is due either to mixing between different feldspar compositions, suggesting exsolution lamellae (Gasda et al., 2016), or sampling between different phases (therefore not a pure feldspar), due to the small grain size (Figure 5b, ~ 1mm) compared to the laser beam size.

Rocks of Group 3 contain alkali-feldspars, mainly anorthoclase but some sanidine as well (Figure 5c). Some light-toned needles are observed in Figure 5d (right). These rocks are the only ones with K-feldspars (Figure 5c), consistent with their significantly higher Rb and Ba content (Figure 6) compared to other measured igneous rocks. Indeed, this merely reflects the frequent substitutions between K, Rb and Ba during crystallization.

In the felsic intrusive rocks of Group 5, anorthite content ranges from 25 to 50%, corresponding to oligoclase-andesine (Figure 5c), with the majority of points within the andesine field (Table 3). All LIBS analyses from the target Ross have sampled a felsic component, ranging from andesine (point 1) to oligoclase (points 2 to 5). Compared to the other groups, rocks from Group 5 present the highest average content in Sr, due to substitutions between Ca and Sr in plagioclase (Figure 6). Figure 5d shows an example of the plagioclase-rich Clinton target, as imaged by the MAHLI instrument. This image shows plagioclase crystals as big as 5 mm that are cut by a dark vein. Grey translucent grains are also observed and may correspond to quartz crystals (Sautter et al., 2015) intergrown with coarse plagioclase grains.

Overall, the main feldspars observed in igneous rocks correspond to andesine, anorthoclase and some sanidine. It is noteworthy that sanidine was also identified in coarse-grained sedimentary rocks analyzed by ChemCam (Le Deit et al. 2016; Mangold et al., 2016a) as well as by CheMin XRD analyses performed at the Kimberley field site in the Windjana fine-grained sandstone (Treiman et al. 2015), which suggests integration of these mineral phases into the sediments.

2-Mafic phases and other phases

Mafic phases are difficult to identify from RMI and MAHLI images, as they have similar color, do not show clear mineral shapes and are usually smaller than light-toned minerals. Therefore, all of the points that did not sample a light-toned crystal (from visual and chemical data) may have probed mafic mixtures of minerals such as pyroxene, olivine, amphibole and oxides with/without trace amounts of feldspar. Corresponding major-element compositions were first broadly filtered to identify mafic mineral candidates, using diagrams such as Figure 4, for all the targets. We first discarded observation points with high Al_2O_3 (> 10%) and K_2O (>1.5%) contents (empirical cutoffs) to screen out any possible contamination from a felsic component. We then selected analyses with SiO_2 values ranging from 40 to 56 wt.%, consistent with pyroxene composition. We finally kept the remaining analyses with decent major-element totals (our guideline is 90 to 105 wt.%).

For this survey of mafic minerals, we excluded Group 3 corresponding to glassy to cryptocrystalline material without any visible dark grains (Figure 4e-f). We then selected all points from Group 2, Group 4 and Group 5 that hit dark phases and/or mesostasis. In the specific case of aphanitic dark-toned rocks of Group 1, it is assumed that pyroxene is the most abundant ferromagnesian phase (Figure 4a), as their crystal structure accommodates all the major elements that occur in basalt with the exception of potassium.

If we assume that the remaining points correspond to relatively “pure” pyroxenes, these points plot strikingly towards the Fe-rich end of the pyroxene quadrilateral (Figure 7 Fs: 0.5-0.9).

Ferro-augites are found in trachyandesites of Group 2 (such as Stock #7 and Horlick #5), quartz-diorites of group 5 (Sparkle #3) and rocks of Group 4 (Elizabeth #4) (Table 4), but a majority of the points plot in the pigeonite field and span a wide range of Mg content between 65 and 25%. This wide range of variation characterizes essentially mafic aphanitic rocks of Group 1 and mafic rocks of Group 4 (Table 4) while Group 2 rocks seem to contain ferro-pigeonites exclusively. Apart from the two ferro-augites observed in Group 5 (Figure 7), mafic analyses in these quartz-diorite rocks (Group 5) generally include some Na and K (< 2% and < 0.3%, resp.), present a low major-element total (90-94%) and show a hydrogen signal. Such compositions have been tentatively recalculated into amphibole for Ruker #6. Nevertheless, hydrogen quantification with ChemCam is still in progress (Rapin et al., 2016; Thomas et al., 2016; Schröder et al., 2015), and the confidence in sampling an amphibole is not yet firmly established. Note that the CheMin instrument used on sedimentary rocks did not observe such Fe-enrichment in pyroxenes (Figure 7), but rather detected Mg-rich augite minerals, as well as Mg-rich pigeonites (Mg# 0.66 and 0.68, respectively, with Mg# corresponding to $Mg/Mg+Fe^{2+}$) and iron oxides (Treiman et al. 2015). Therefore, igneous pyroxenes at Gale seem to be iron-rich (Table 4) when compared to sediments analyzed by CheMin during the rover traverse.

Johnson et al (2015) focused on the passive spectra from ChemCam. Some of their data points correspond to igneous targets that are included in our study, such as Ashuanipi and La_Reine, from Group 4. From their study, it is interesting to note that they attributed the downturn observed in the spectra after 750 nm to the possible presence of orthopyroxenes or other low-Ca pyroxenes. Our pyroxene analysis of Ashuanipi (Figure 7, Table 4) points toward low-calcium pyroxene, consistent with the overall interpretation of Johnson et al (2015).

Analyses that are left over after this screening have low totals (lower than 90%) and low SiO_2 contents (usually < 40%), and correspond to potential mixtures of oxides and olivine that are hard to untangle. As mentioned above, if olivine precipitated in these rocks, it should have formed tiny crystals that would be invisible at the RMI scale (in contrast to the macroscopic olivine grains found in Bagnold Dunes; e.g., Ehlmann et al., 2016; Cousin et al., 2016). Such oxide-dominated mixtures (Table 5) have been detected within the five rock types described in the present paper. In Group 1, they correspond to analyses depleted in SiO_2 (SiO_2 < 40 wt.%) compared to the other analyses within this group, but enriched in TiO_2 (1.2 < TiO_2 <1.5 wt.%) with high FeO_T contents (24 < FeO_T < 36 wt.%) and low MgO (<3 wt.%), such as in Watterson #9. They could represent ilmenite-dominated mixtures. These points also show enrichment in Cr (Figure 6). Similar mixtures have been observed in Group 2 rocks such as Horlick #4, and in intrusive fine-grained rocks of Group 4 such as Beacon #6. Their SiO_2 content is lower than 41 wt.%, TiO_2 ranges from 1.2 to 4 wt.% and FeO_T varies from 20 to 28 wt.%. Harrison #5 is somewhat special with very high FeO_T (40 wt.%) correlated with a high Mn signal (corresponding to ~ 40 wt.% MnO), both decreasing with depth. This point likely corresponds to a mixture with a Fe/Mn oxide coating that could be more or less hydrated (the hydrogen line also decreases with depth) (Lanza et al 2014). A few Fe-Ti oxides have also been detected in leucocratic aphanitic Group 3 rocks (Chakonipau #3, where TiO_2 goes up to 13 wt.%). Only one point from the leucocratic intrusive rocks of Group 5 seems to be an oxide mixture (Noriss_2 #6), with almost 3 wt.% TiO_2 and 20 wt.% FeO_T.

Some other accessory phases corresponding to F-bearing minerals (Forni et al. 2015) have been detected in rocks of Groups 1, 2 and 4. Among the porphyritic rocks, the dark point Harrison #4 contains approximately 1 wt.% F and is enriched in CaO (up to 16 wt.%); shot-to-

shot analysis shows a correlation between the F and the CaO contents (Forni et al., 2015). This point also reveals Cl and P spectral signatures suggesting that a Cl-F apatite crystal has been sampled. Some other points contain up to 1 wt.% F, such as Blackhead #7 from Group 1 aphanitic dark rocks that also contains > 15 wt.% CaO and displays a P spectral signature, thus suggesting the presence of a F-apatite crystal. Finally, a few points in fine-grained rocks (Group 4) could contain some micas or amphibole, as the F signal is correlated with the Li, Mg & Si signatures (Black_Trout #1 and Ashuanipi #2).

To summarize the discussion on the mineralogy of the igneous rocks observed at Gale, concerning the felsic phases, rocks of Groups 1 and 4 as well as Group 2 porphyritic rocks contain mainly andesine, and rocks of Group 5 include andesine-oligoclase, whereas rocks of Group 3 are dominated by orthoclase and sanidine. Moreover, mafic minerals contained in all these groups are more Fe-rich and Mg-poor than most of the martian shergottites. Except for some points that hit nearly ‘pure‘ pyroxene phases (Table 4), we analyzed mineral mixtures that included pyroxene, oxides, apatite, and potentially amphibole. Pyroxenes are displayed toward the $Ca\text{-}Fe^{2+}$ – $Fe^{2+}Fe^{3+}$ (ferrosillite) side of the quadrilateral, giving rise to ferro-augite and ferro-pigeonite consistent with evolved low-temperature (900 – 1000 °C) host rocks (Lindsley et al. 1983), and therefore corresponding to a late stage in the crystallization sequence.

VI. Petrology

All the characteristics of each group of rocks (number of observations, texture, mineralogy and rock type) are summarized in Table 7.

Groups 2, 3 and 5 being already well described in term of petrology in previous papers (Sautter et al. 2014, 2015, 2016), this study focuses on the two other groups that are newly observed on Mars: effusive aphanitic dark rocks (Group 1) and intrusive fine-grained rocks (Group 4). For the 20 rocks with aphanitic texture (Group 1), representative whole-rock estimates (Table 6) can be obtained by averaging all locations for each rock, since the grain size is smaller than the laser beam size. On the other hand, the whole rock composition of fine-grained intrusive rocks (Group 4) is more difficult to assess. These rocks have grains up to the laser beam size, but no obvious pure phases have been sampled (see part V), making the modal reconstruction difficult and not accurate. Therefore, for these rocks of Group 4, only targets with at least 9 observation points are taken into account (La Reine, Eagle Mountain, Ashuanipi and Black Trout).

On a total alkali-silica (TAS) diagram (Figure 8a), the dark aphanitic rocks of Group 1 show two sub-groups depending on their alkali content. Alkali-poor rocks of Group 1 plot in the picro-basalt (Pyramid_Hills) and basalt (for example, Watterson and Gunflint) fields while alkali-rich targets of Group 1 are in the tephrite (Johnnie) and trachy-basalt (Timble) domains. Considering all the Group 1 rocks together they show variable Mg#s (Table 6) ranging from strikingly low values (Mg# 0.15 in Watterson) to high values (Mg# 0.46 in Gunflint, Mg# 0.44 in Johnnie). Such variations are highlighted by pyroxene compositions in § V.2. Even if the presence of Fe-oxides could contribute to these low Mg#s, in most cases oxides have not been obviously sampled, and the normative ilmenite/hematite components are the same for the rocks with low Mg# and for the rocks with a higher Mg# (Table 6). They all contain normative olivine, although olivine as a phenocryst phase has not yet been observed at Gale in igneous rocks.

However, ferroan bulk compositions typically produce abundant fine-grained intergrowths of fayalite, hedenbergite and tridymite by breakdown of pyroxferroite, as first discovered in lunar mare basalts (Lindsley et al. 1972), and later in the most differentiated basaltic shergottites such as Los Angeles and Queen Alexandra Range (QUE 94201) (Rubin et al. 2000, Mikouchi 2001, Warren et al. 2004). Normative olivine could merely indicate that fayalite needles are not detectable by ChemCam. Moreover, all targets of Group 1 have high contents of normative feldspars (an average of ~ 45% plagioclases, ~ 8% K-feldspars), which indicate an abundance of feldspar microliths that are unfortunately too small to provide clean ChemCam analyses (see §V-1). The subgroup of rocks with a higher alkali content contain up to 8% normative nepheline, which could suggest the presence of feldspathoids instead of feldspars. This would be consistent with the low Si content observed in these rocks (see part IV and Table 6).

Concerning rocks of Group 4, as in Group 1, the most variable elements are FeO_T and MgO, with Mg# (Table 6) ranging from 0.26 in Eagle-Mountain to 0.56 in La Reine. The normative composition contains ~ 48% plagioclase, ~ 2-10% orthoclase, ~ 30-35% pyroxene (mainly low-calcium pyroxene), ~ 5-19% olivine and ~ 1-3% ilmenite. Such normative compositions, together with observed textures, are consistent with gabbro-norite classification.

The rocks of Group 2, also called "trachyandesites" by Sautter et al. (2015), included seven distinct samples with markedly heterogeneous compositions (Gini index). Since the grain sizes are larger than the laser beam, its composition had been estimated from the only rock sampled with a large raster (4x4): Harrison (Sautter et al. 2015). Yet, this present study extends this group with two new porphyritic rocks: Airfield and Albee. Nevertheless, only five points were observed on Airfield, and all nine points from Albee sampled the plagioclase phenocrysts, precluding whole-rock compositional assessment. These porphyritic rocks are well represented in Gale (17% of the igneous rocks observed by ChemCam), but unfortunately their heterogeneous textures make their analyses difficult by rasters with limited numbers of points.

This present study expands Group 3 described as "trachytes" in Sautter et al. (2015), with one rock called Meeting House. The normative composition gives 10% quartz, 55% plagioclase (An <10), 23% orthoclase, 4% diopside and 8% hypersthene, with 1% ilmenite, consistent with previously described trachytic rocks (Group 3: Sledgers, Chakonipau and Becraft). Whole-rock calculations for Blanchet and Stark are not possible, as no analyses have been acquired for Blanchet and only one for Stark.

Note that in the present survey we did not find any new rocks after sol 500 belonging to Group 5 described as quartz-diorite rocks in Sautter et al (2015), indicating that these rocks are concentrated in the vicinity of the alluvial fan deposit below the Peace Vallis channel.

VI. Discussion

Gale crater rocks expand the diversity of igneous rocks that make up the Martian crust beyond the composition at any other landing site as well as the composition of the vast majority of Martian meteorites excepted the polymict breccia NWA 7034 (Santos et al. 2015, McCubin et al. 2016) and its paired samples (NWA 7533 - Humanyun et al. 2015, Hewins et al. 2016).

Igneous composition through the MSL traverse

Basaltic rocks are very well represented (34% of the igneous rocks - Figure 9a) and include iron-rich and magnesium-poor specimens. The second most common group of rocks corresponds to the dioritic rocks of Group 5 (up to 20%). Gabbro together with trachyandesites, are the third most abundant types of igneous rocks observed along the traverse, representing each 17% of the total. Finally trachyte contribution is 10%. If we gather all the rocks with more than 50 wt.% feldspar crystals (diorites, trachytes and trachyandesites), they correspond to 49% of all the igneous rocks, which means that feldspar-rich lithologies are widespread at Gale crater. Interestingly potassium-rich and silica-rich sediments have been found at Gale crater, respectively at Kimberley (LeDeit et al., 2016) and Maria Pass (Morris et al., 2016).

Felsic and mafic rocks do not seem however to be distributed randomly on the crater floor along the Curiosity traverse (Figure 9b). Felsic rocks (diorites, trachytes and trachyandesites) have been observed mostly close to the Bradbury landing site during the first 20 months of the mission (sols 13 to 552). The landing site is located to the south of the alluvial fan at the mouth of Peace Vallis (Palucis et al., 2014), a river channel that cuts through the northern rim of Gale crater. This felsic component has also been observed among the conglomerates near the landing site (Mangold et al., 2016a). The occurrence of felsic rocks as rounded float rocks associated with conglomerates, or forming distinctive clasts within them along with felsic pebbles and coarse grains of similar composition (Meslin et al., 2013; Cousin et al., 2014; Cousin et al., 2015), indicate that they are the product of mechanical weathering of conglomerates. Felsic rocks would have been sampled initially by the Peace Vallis river within an evolved magmatic sequence through a vertical section on the order of 3 km thick exposed in Gale crater's walls. Then they would accumulate as alluvial deposit on Gale crater floor (Sautter et al. 2015, 2016). Note that such a deep crustal sequence remain hidden from remote orbital optical and infrared spectroscopy which analyze exclusively the upper most part of the basaltic regolith (Bibring et al. 2005, Christensen et al. 2001).

Mafic and intermediate rocks (basalts and gabbros) have been observed all along the traverse up to sol 800, but they increase in number after the Kimberley outcrop (after sol ~ 630) as the rover drove away from the alluvial fan and approached Mount Sharp. Consequently these mafic lithologies do not seem directly related to the Peace Vallis alluvial fan deposit, but appear to be the most common igneous rock type analyzed so far at Gale. As the mafic rocks are float without clear stratigraphic context, their exact location within the complex sedimentary stratification on Gale crater's floor or in the regional geologic landscape is difficult to assess. However, these mafic rocks have been interpreted as having been formed before the sedimentary sequence described in the literature (Grotzinger, 2015; Anderson, 2013; Le Deit 2016; Vaniman 2015; Treiman 2016). Interestingly, the main sedimentary groups have Mg 's number varying between 15 and 60 (Bridges et al. 2016) similar to mafic igneous rock compositions (14 to 50 for Group 1 and 26 to 56 for Group 4) and thus could represent their erosional and relithified product (Bridges et al., 2016). However, K-rich sediments at Kimberley (Treiman et al. 2016; Le Deit et al. 2016) and detrital (high-temperature) tridymite at Marias Pass in the Murray formation (sol 991-993, Morris et al. 2016) have been observed, which indicate potentially complex sedimentary histories that are not directly related to this simplistic hypothesis of erosion, deposition, and lithification of mafic materials in a lacustrine environment. This indicates different volcanic sources, potassic and silica-rich, at or near Gale crater.

What is the relationship if any, between these basaltic rocks (Group 1-4) and the alkaline suite (Group 2-3)? The alkali trend described in Sautter et al. (2015), indicated by the black

dashed line in Figure 8a, was interpreted as fractionated liquids at 1 bar of a primary melt with Black-Trout (Group 4) composition (Mg# 0.28) produced at 1 GPa from a low degree of partial melting (6%) of primitive Martian mantle using Dreibus and Wanke (1986) composition. The present survey of mafic rocks (Groups 1 & 4) in Gale shows however a wide range of textures and compositions varying from alkali-poor to alkali-rich end-members, with iron-rich compositions and variable Mg#. Given the lack of olivine phenocrysts and variable Mg number between 15 and 50 (Table 6), they cannot be all primary basalts derived from the primitive mantle.

Comparison with MER igneous rocks compositions

The new rock types of the basanite/basalt group (Group 1) and micro gabbro and norite (Group 4), when plotted in a TAS diagram (Figure 8a), are within the fields of Columbia Hills alkali basalts and basaltic rocks from Gusev crater. However Group 1 basalts do not contain olivine phenocrysts and are more iron-rich (Mg# < 0.5 between 0.15 and 0.5, Table 6) compared to the vast majority of basaltic rocks analyzed by Spirit and Opportunity. Adirondack class olivine-rich basalts have a Mg# between 0.51 and 0.55, while the relatively unaltered alkaline rocks from Columbia Hills (Backstay, Irvine and Wishstone) have Mg#s of 0.53, 0.46 and 0.40, respectively (McSween et al., 2006a, 2006b; Squyres et al., 2006). This difference is highlighted in a MgO/FeO_T vs. Al_2O_3/SiO_2 diagram in Figure 8b where 70% of the mafic rocks analyzed at Gale have MgO/FeO_T less than 0.4 while Gusev rocks plot above this value. Another observation is that for a given value of MgO/FeO_T around 0.2, Al_2O_3/SiO_2 ratios in Gale are scattered between 0.17 and 0.4. Such variations are more likely due to ChemCam's random sampling of fine-grained rocks having a heterogeneous distribution of microliths within glassy mesostasis at a scale lower than the spatial resolution of the laser beam and the RMI. High Al_2O_3/SiO_2 values (> 0.25) would consequently reflect a bias due to preferential sampling of feldspar microliths in some of the rock targets rather than a genuine variation in whole-rock chemistry. If so, the nepheline-normative rocks of Group 1 may not correspond to a distinctive rock sub-class in Gale but may merely reflect this sampling bias by ChemCam.

Adirondack olivine basalts (with ~Mg# 0.53) are primary basalt thought to represent unfractionated primitive magma compositions formed by high degrees of partial melting (15-20%) of a primitive mantle source (with Mg# 0.75-0.8 from Dreibus and Wänke 1986) at ~ 85 km depth and 1 GPa (McSween et al. 2006b). The different set of lithologies observed later at Columbia Hills (Wishstone, Irvine and Backstay), are mildly alkaline in composition (alkaline basalts and tephrites) and thought to be related through fractional crystallization of Adirondack magma at various depths (McSween et al. 2006a). Basaltic rocks_of Group 1 are more geochemically evolved compared to Gusev basalts. They could represent parental–melt of Mg-rich pyroxene cumulates, but such rocks have never been observed at Gale. Alternatively all those basalts with variable Mg number could have sampled heterogeneous mantle i.e. compositionally distinct sources at depth, which seems unlikely, as they have been found within a very small perimeter. Also, assimilation of Iron-rich sediments cannot be excluded.

Comparison with Martian meteorites

Concerning the mineralogy of the Gale igneous rocks, the main feldspars observed correspond to andesine, anorthoclase and some sanidine, which is similar to most of the feldspars observed in the basaltic and trachyandesite clasts of NWA 7034 (Santos et al., 2015). The difference observed comes from the sanidine, which is more enriched in K in NWA 7034 compared to sanidine observed in Group 3 rocks at Gale. The pyroxene compositions observed in our study are not uncommon on Mars. They have been previously found in mars meteorites, both in a few basaltic shergottites (Los Angeles with pyroxenes $Fs_{45\text{-}95}$, NWA 480, QUE 94201 - Mikouchi et al., 2001; Warren et al., 2003) and in nakhlites (Mikouchi et al., 2003, Treiman et al., 2004). In the latter, augite phenocrysts are enriched in iron in contact with iron–rich mesostasis (including ferro-pigeonite, fayalite) (Treiman 2004 and references therein).

Gale crater evolved basalts of Group 1 differ from the vast majority of Martian meteorites. Most of them are mafic and ultramafic cumulates and the rare shergottites that could represent primary basaltic melt are generally olivine-phyric shergottites (Y980497, NWA 5789, LAR 06319, NWA 2990) with high Mg# and olivine phenocrysts (Shirai et al., 2004; Irving et al., 2010; Shafer et al., 2009; Bunch et al., 2009). Interestingly iron-rich basaltic composition of Watterson is similar to the Nakhlite parental magma (NPM) (Stockstill et al. 2005, Sautter et al. 2012), for which the most accepted values, referred as NA03 and NPM05, have a low Mg# (~0.23). Calcium is higher in those experimentally rehomogenized melt inclusions as, during heating experiments, dissolution of some augite hosting the inclusion may have occurred (Sautter et al. 2012). The normative compositions of nakhlite parental magma and Gale iron-rich basalts (Table 6) indicate that they cannot be the product of melting of a typical, not metasomatized mantle (i.e. a mixture of dominant olivine, pyroxene and minor plagioclase). These particular melt compositions result from a strong iron enrichment in the source, which makes olivine far more fusible than in more MgO rich sources, or possibly this melt already fractionated to a significant extent. Udry et al. (2014a) performed pMELTs and MELTs fractional crystallization calculations that followed a polybaric path (fractionation at medium pressure followed by sub-adiabatic ascent) on Nakhlite parental magma compositions (NA03). Starting from 1.25 GPa and 1300-1380°C under dry conditions, they obtained a residual liquid extending into the alkaline field toward trachyte compositions. Initially, SiO_2 and FeO_T increase followed by a decrease in FeO_T due to olivine fractionation at high and low pressures. Feldspar crystallization is responsible for a decrease in Al_2O_3 abundance starting after 30% fractionation. The only pyroxene to crystallize is augite, so the residual liquid shows a continuous decrease in CaO. The iron-rich Watterson type of basalt could therefore be the mafic end-member of the calculated liquid line of descent (Sautter et al. 2015) passing through Black-Trout (dashed line in Figure 8a) which parallels the liquid line of descent calculated by Udry et al. (Figure 11 in Udry et al., 2014a). Consequently, fractionation at a depth of 70 km of a magma originating at 90 km depth, followed by sub-adiabatic ascent under anhydrous conditions, could have caused the magmatic evolution towards alkaline compositions observed at Gale. It is interesting to note that ferroan lunar basalt Asuka-881757 also crystallized from dry magma (Mikouchi 2001), which could suggest similar formation conditions of these two samples, even if they come from two different planetary bodies.

Group 4 micro-gabbros with Mg# between 0.25 and 0.55 look like gabbroic shergottites such as Los Angeles, QUE 94201 (Rubin et al. 2000, McSween et al. 1999) and NWA 7320 (Udry et al. 2016) which have lower Mg# than olivine-bearing shergottites. Los Angeles is the most geochemically evolved martian sample with the lowest Mg# (0.14) than any other martian

meteorites. Rather than being a primary melt from a plausibly heterogeneous mantle that elsewhere generate more Mg-rich magma, Los Angeles has been interpreted as a part of shallow intrusion proceeded by an episode of fractional crystallization and /or assimilation of older crustal matter (Rubin et al. 2000). Black-Trout (Mg# 0.28) and Eagle-Montain (Mg# 0.26) intrusive micro gabbro of Group 4 could result from the same processes.

The new polymict breccia NWA 7034 and pairings so far identified NWA 7533, 7475, 7906, 7907, 8114, 8171 (Agee et al. 2013, Humayun et al. 2013, Santos et al. 2015, Hewins et al. 2016, McCubbin et al. 2016) contain basalt, trachyandesite, basaltic andesite and FTP clasts (Santos et al. 2015). However the majority of these effusive clasts have higher Mg# (Mg# > 0.50) compared to Gale crater basalts. Iron rich clasts are limited to one basalt clast (clast 77) due to the Ca-Fe –rich nature of its pyroxene and a FTP clast with Mg# as low as 0.10. The latter is peculiar being pyroxene-free and rich in Fe-Ti oxides. This more likely does not correspond to a real rock composition but rather reflect preferential sampling of oxide phases in a host rock that would have very heterogenous modal repartition. All FTP clasts are very small and show variable modal composition from one clast to the other.

VII. Conclusion

Overall, the *in situ* data from Gale crater provide unprecedented insights into the diversity of igneous rocks at the surface of Mars. ChemCam analyzed a total of 59 effusive and intrusive igneous rocks during the traverse up to sol 800 ranging from picritic to trachytic compositions. This variety was not expected from the results obtained during the previous *in situ* missions, but these observations are consistent with those from the new meteorite NWA 7533 (Humayun et al., 2013) and paired samples NWA 7034 (Agee et al. 2013, Santos et al. 2015) and from recent orbital observations, summarized in Sautter et al. (2016).

The Curiosity imagers allowed the distinction between intrusive and effusive igneous rocks, which is important information for petrological processes. Among the feldspars, we have sampled mainly andesine and anorthoclase, as well as some sanidine. Pyroxenes are iron-rich and rather low in calcium, consistent with passive observations as well. Secondary phases have been observed, such as Fe/Ti-oxides and apatites.

Gale basaltic rocks show distinct compositions compared to the igneous rocks analyzed by the Spirit rover in Gusev crater. Most of them show a low Mg# (<0.5), which could be explained either by a different mantle reservoir between these landing sites, or by a more extensive fractional crystallization concerning the Gale basaltic rocks. From our study, we propose that rocks from Group 1 such as Watterson basalt could be the mafic end-member of the alkaline trend observed at Gale. Magma originating at low depth followed by fractional crystallization with sub-adiabatic ascent under anhydrous conditions could have caused the magmatic evolution towards alkaline compositions observed at Gale.

These igneous rocks are not randomly distributed along Curiosity's traverse; rather, the felsic targets (trachyandesites, trachytes and quartz-diorites) have been observed near the landing site, close to the Peace Vallis alluvial fan. These targets seem to have been transported by fluvial

activity and therefore represent a sampling from the crater northern rim, while the mafic targets such as the basalts and the gabbros are mainly observed later on the traverse.

Basalts represent the main type of igneous rocks sampled by ChemCam along the traverse. Nevertheless, the second most common igneous rocks correspond to the quartz-diorites. Moreover, the felsic igneous rocks all together represent up to 49% of the observed igneous rocks, meaning that feldspars are widespread at Gale crater.

While the *in situ* data from Gale crater provide unprecedented insights into the diversity of igneous rocks at Gale crater and, by extension, on the surface of Mars, a lot remains to be learned concerning the diversity of igneous rocks before it is possible to arrive at a complete understanding of the ancient Martian magmatism and its variations over time.

ACKNOWLEDGEMENTS

The engineers and scientists who developed and operated the Curiosity rover are thanked for their generous contributions to this work. This work was supported by CNES in France and by the Mars Exploration Program in the US.

REFERENCES

Agee C. B., Wilson N. V., McCubbin F. M., Ziegler K., Polyak V. J., Sharp Z. D., Asmerom Y., Nunn M. H., Shaheen R., Thiemens M. H., Steele A., Fogel M. L., Bowden R., Glamoclija M., Zhang Z., Elardo S. M. 2013. Unique Meteorite from Early Amazonian Mars: Water-Rich Basaltic Breccia Northwest Africa 7034. *Science, Volume 339, Issue 6121, pp. 780-785. DOI: 10.1126/science.1228858*

Anderson R. B., Clegg S. M., Frydenvang J., Wiens R. C. McLennan S., Morris R. V., Ehlmann B., and Dyar M. D. (2016) Improved accuracy in quantitative laser-induced breakdown spectroscopy using sub-model partial least squares. *Submitted to Spectrochim Acta*.

Bandfield J. L., Hamilton V. E., Christensen P. R., McSween H. Y., 2004. Identification of quartzofeldspathic materials on Mars. *Journal of Geophysical Research, Volume 109, Issue E10. DOI: 10.1029/2004JE002290*

Bandfield J. L. 2006. Extended surface exposures of granitoid compositions in Syrtis Major, Mars. *Geophysical Research Letters, Volume 33, Issue 6. DOI: 10.1029/2005GL025559*

Bell III, J. F., M. C. Malin, M. A. Caplinger, M. A. Ravine, A. S. Godber, M. C. Jungers, M. S. Rice, R. B. Anderson (2012), Mastcam multispectral imaging on the Mars Science Laboratory rover: Wavelength coverage and imaging strategies at the Gale Crater field site, *43th Lunar Planet. Sci. Conf. abstract 2541.*

Blake D., Vaniman D., Achilles C., Anderson R., Bish D., Bristow T., Chen C., Chipera S., Crisp J., Des Marais D., Downs R., Farmer J., Feldman S., Fonda M., Gailhanou M., Ma H., Ming D., Morris R., Sarrazin P., Stolper E., Treiman A., Yen A. (2012) Characterization and calibration of the CheMin Mineralogical Instrument on Mars Science Laboratory. *Space Science Review 170, 341-399.*

Blaney D., Wiens R.C., Maurice S., Clegg S.M., Anderson R.B., Kah L.C., Le Mouelic S., Ollila A., Bridges N., Tokar R., Berger G., Bridges J., Cousin A., Clark B., Dyar M.D., Ehlmann B., King P.L., Lanza N., Mangold N., Meslin P.-Y., Newsom H., Schroeder S., Rowland S., Johnson J., Edgar L., Gasnault O., Forni O., and the MSL Science Team (2014) Chemistry and texture of the rocks at "Rocknest", Gale crater: Evidence for iron-rich cements. *J. Geophys. Res., 119, 2109-2131, DOI: 10.1002/2013JE004590.*

Bridges J. C., Edwards P. H., Anderson R., Dyar M. D., Fisk M., Thompson L., ... & Filiberto, J. (2016). Igneous differentiation on Mars: trachybasalts in Gale crater. In *Lunar and Planetary Science Conference* (Vol. 47, p. 2160).

Bunch T.E., Irving A.J., Wittke J.H., Rumble D., Korotev R.L., Gellissen M. and Palme H. (2009) Petrology and composition of Northwest Africa 2990: A new type of fine-grained enriched, olivine-phyric Shergottite. In *Lunar and Planetary Science Conference* (Vol. 40, p. 2274).

Campbell J.L., Perrett G.M., Gellert R., Andruskenko S.M., Boyd N.I., Maxwell J.A., King P.L., Schofield C.D.M., (2012). Calibration of the Mars science laboratory alpha particle X-ray spectrometer. *Space Science Review 170, 319–340.*

Carter J. and Poulet F., 2013. Ancient plutonic processes on Mars inferred from the detection of possible anorthositic terrains. *Nature Geoscience, Volume 6, Issue 12, pp. 1008-1012. DOI: 10.1038/ngeo1995.*

Clegg S. M., Sklute E., Dyar M. D., Barefield J. E., & Wiens R. C. (2009). Multivariate analysis of remote laser-induced breakdown spectroscopy spectra using partial least squares, principal component analysis, and related techniques. *Spectrochimica Acta Part B: Atomic Spectroscopy, 64*(1), 79-88.

Clegg S., Wiens R., Anderson R., Forni O., Frydenvang J., Lasue J., Cousin A., Payré V., et al. Recalibration of the Mars Science Laboratory ChemCam Instrument with an Expanded Geochemical Database, *submitted to Spectrochimica Acta part B.*

Cousin A., Meslin P. Y., Wiens R. C., Rapin W., Mangold N., Fabre C., Gasnault O., Forni O., Tokar R., Ollila A. , Schroeder S. , Lasue J. , Maurice S. , Sautter V. , Newsom H. , Vaniman D. , Le Mouélic S. , Dyar D. , Berger G. , Blaney D. ,Nachon M. , Dromart G. , Lanza N. , Clark B. , Clegg S. , Goetz W. , Berger J. , Barraclough B. , Delapp D. 2014. Chemistry of Coarse Particles in Soils and Their Relationship with Local Rocks, *Eighth International Conference on Mars, n. 1095.*

Cousin A., Meslin P. Y., Wiens R. C., Rapin W., Mangold N., Fabre C., ... & Schröder S. (2015). Compositions of coarse and fine particles in martian soils at gale: A window into the production of soils. *Icarus, 249,* 22-42.

Cousin A., Forni O., Meslin P. Y., Schroeder S., Gasnault O., et al (2016). Chemical Diversity Among Fine-Grained Soils at Gale (Mars): A Chemical Transition as the Rover is Approaching the Bagnold Dunes? In *Lunar and Planetary Science Conference (Vol. 47, p. 2044).*

Dray, J.M.D., Taylor, C.L. Floss, A. and Mc Sween H.Y. (2006) Petrology and chemistry of MIL 03346 and its signific&nce in understanding the petrogenesis of Nakhlites on Mars. *Meteorit. Planet. Sci., 41, 581-606.*

Dreibus G., & Wanke H. (1985). Mars, a volatile-rich planet. *Meteoritics, 20, 367-381.*

Edgett K. S., & Yingst R. A. (2013). Curiosity's Mars Hand Lens Imager (MAHLI): Sol 0–179 activities, observations, range and scale characterization. In *European Planetary Science Congress (Vol. 8, pp. EPSC2013-246).*

Edwards P.H., Bridges J.C., Wiens R.C., Anderson R., Dyar M.D., Fisk M., Thompson L., Gasda P., Filiberto J., Schwenzer S.P., Blaney D., and Hutchinson I. (2016) Basalt-trachybasalt samples from Gale crater, *Mars. Submitted to Met. Planet. Sci.*

Ehlmann B., Bridges N., Fraeman A., Lapotre M., Edgett K. et al (2016). Chemistry and Mineralogy In Situ at the Bagnold Sand Dunes: Evidence for Aeolian Sorting and Size-Dependence in Sand Composition. In *Lunar and Planetary Science Conference (Vol. 47, p. 1536).*

Eliazar I. I., & Sokolov I. M. (2010). Gini characterization of extreme-value statistics. *Physica A: Statistical Mechanics and its Applications, 389(21), 4462-4472.*

Fabre, C., Maurice, S., Cousin, A., Wiens, R. C., Forni, O., Sautter, V., & Guillaume, D. (2011). Onboard calibration igneous targets for the Mars Science Laboratory Curiosity rover and the Chemistry Camera laser induced breakdown spectroscopy instrument. *Spectrochimica Acta Part B: Atomic Spectroscopy, 66(3), 280-289.*

Forni O., Clegg S., Wiens R. C., Maurice S., & Gasnault O. (2009). Multivariate analysis of ChemCam first calibration samples. In *Lunar and Planetary Science Conference (Vol. 40, p. 1523).*

Forni O., Maurice S., Gasnault O., Wiens R. C., Cousin A., Clegg S. M., ... & Lasue J. (2013). Independent component analysis classification of laser induced breakdown spectroscopy spectra. *Spectrochimica Acta Part B: Atomic Spectroscopy, 86, 31-41.*

Forni O., Gaft M., Toplis M. J., Clegg S. M., Maurice S., Wiens R. C., ... & Meslin P. Y. (2015). First detection of fluorine on Mars: Implications for Gale Crater's geochemistry. *Geophysical Research Letters, 42(4), 1020-1028.*

Gasda P. J., Delapp D. M., McInroy R. E., Wiens R. C., Bridges J. C., Edwards P. H., ... & Clegg S. (2016). Identification of Fresh Feldspars in Gale Crater Using ChemCam. In *Lunar and Planetary Science Conference (Vol. 47, p. 1604).*

Gini C. (1921). Measurement of inequality of incomes. *The Economic Journal, 31(121), 124-126.*

Grotzinger J. P., Sumner D. Y., Kah L. C., Stack K., Gupta S., Edgar L., ... & Milliken R. (2014). A habitable fluvio-lacustrine environment at Yellowknife Bay, Gale Crater, Mars. *Science, 343(6169), 1242777. DOI: 10.1126/science.1242777*

Grotzinger J. P., Gupta S., Malin M. C., Rubin D. M., Schieber J., Siebach K., ... & Calef F. (2015). Deposition, exhumation, and paleoclimate of an ancient lake deposit, Gale crater, Mars. *Science, 350.*

Hewins R. H., Zanda B., Humayun M., Leroux H. (2016). NWA 7533: An Overview of Melt Rocks and Breccia Assembly History. In *79th Annual Meeting of the Meteoritical Society No. 1921, id.6366.*

Humayun M., Nemchin A., Zanda B., Hewins R. H., Grange M., Kennedy A., Lorand J.-P., Göpel C., Fieni C., Pont S., Deldicque D. (2013). Origin and Age of the Earliest Martian Crust from Meteorite NWA 7533. *Nature, Vol. 503, pp. 513-516.*

Humayun M., Hewins R. H., Zanda B. (2014). Weathering, Transport and Impact Melting in the Martian Highlands Crust Viewed from Martian Meteorite NWA 7533. *Mars 8th conference, # 1791, p.1459.*

Hyvarinen A. (2001). Blind source separation by nonstationarity of variance: a cumulant-based approach. *Neural Networks, IEEE Transactions on, 12(6), 1471-1474.*

Irving A.J., Kuehner S.M., Herd C.D.K., Gellissen M., Korotev R.L., Puchtel I., Walker R.J., Lapen T.J., Rumble D (2010) Petrologic, Elemental and Multi-isotopic Characterization of Permafic Olivine-Phyric Shergottite Northwest Africa 5789: A Primitive Magma Derived From Depleted Martian Mantle. In *Lunar and Planetary Science Conference (Vol. 41, p. 1547).*

Johnson J. R., Bell III J.F., Bender S., Blaney D., Cloutis E., DeFlores L., Ehlmann B., Gasnault O., Gondet B., Kinch K., Lemmon M., Le Mouélic S., Maurice S., Rice M., Wiens R., MSL Science Team (2015). ChemCam Passive Reflectance Spectroscopy of Surface Materials at the Curiosity Landing Site, Mars, *Icarus, 249, 74–92, http://dx.doi.org/10.1016/j.icarus.2014.02.028.*

Langevin, Y. et al., (2013). Processing approaches for optimal science exploitation of the ChemCam Remote Microscopic Imager (RMI) during the first 90 days of curiosity operations. *Lunar Planet. Sci. 44. Abstract 1227.*

Lanza N. L., Fische, W. W., Wiens R. C., Grotzinger J., Ollila A. M., Cousin A., ... & Maurice S. (2014). High manganese concentrations in rocks at Gale crater, Mars. *Geophysical Research Letters, 41(16), 5755-5763.*

Lasue J., Wiens R. C., Stepinski T. F., Forni O., Clegg S. M., & Maurice S. (2011). Nonlinear mapping technique for data visualization and clustering assessment of LIBS data: application to ChemCam data. *Analytical and bioanalytical chemistry, 400(10), 3247-3260.*

Le Deit L., et al. (2016), The potassic sedimentary rocks in Gale Crater, Mars, as seen by ChemCam on board Curiosity, J. Geophys. Res. Planets, 121, doi:10.1002/2015JE004987.

Le Mouélic, S., Gasnault, O., Herkenhoff, K. E., Bridges, N. T., Langevin, Y., Mangold, N., ... & Deen, R. G. (2015). The ChemCam Remote Micro-Imager at Gale crater: Review of the first year of operations on Mars. *Icarus, 249, 93-107.*

Lindsley D. H., & Andersen D. J. (1983). A two-pyroxene thermometer. *Journal of Geophysical Research: Solid Earth, 88(S02).*

Lindsley D.H. , Papike, J.J., and Bence, A.E. (1972): Pyroxferroite: Breakdwon at low pressure and high temperature. *Lunar Sci. Inst., 483-485.*

Le Mouélic, S., O. Gasnault, K.E. Herkenhoff, N.T. Bridges, Y. Langevin, N. Mangold, S. Maurice, R.C. Wiens, P. Pinet, H.E. Newsom, R.G. Deen, J.F. Bell III, J.R. Johnson, W. Rapin, B. Barraclough, D.L. Blaney, L. Deflores, J. Maki, M.C. Malin, R. Pérez, M. Saccoccio, et al, (2015*)* The ChemCam Remote Micro-Imager at Gale crater: Review of the first year of operations on Mars, *Icarus, 249, 93-107, DOI: 10.1016/j.icarus.2014.05.030.*

Malin M. C., Caplinger M. A., Edgett K. S., Ghaemi F. T., Ravine M. A., Schaffner J. A., ... & Willson R. G. (2010). The Mars Science Laboratory (MSL) mast-mounted cameras (Mastcams) flight instruments. In *Lunar and Planetary Science Conference (Vol. 41, p. 1123).*

Mangold N., Forni O., Dromart G., Stack K., Wiens R. C., Gasnault O., Sumner D., Nachon M., Meslin P. Y., Anderson R., et al. (2015) Chemical variations in Yellowknife Bay formation sedimentary rocks analyzed by ChemCam on board the Curiosity rover on Mars. *Journal of Geophysical Research Planets 120 (3) 452-482.*

Mangold N., Thompson L. M., Forni O., Williams A. J., Fabre C., Le Deit L., ... & Calef F. (2016a). Composition of conglomerates analyzed by the Curiosity rover: Implications for Gale Crater crust and sediment sources. *Journal of Geophysical Research: Planets, 121* (3*), 353-387.*

Mangold N., Schmidt M. E., Fisk M., Forni O., McLennan S., Ming D., Sautter V., Sumner D., Williams A., Clegg S., Cousin A., Gasnault O., Gellert R., Grotzinger J., Wiens R. (2016b) Classification scheme for sedimentary and igneous rocks un Gale crater, Mars. *Submitted to Icarus, July 2016.*

Manville V., Segschneider B., Newton E., White J. D. L., Houghton B. F., Wilson C. J. N. (2009). Environmental impact of the 1.8 Ka Taupo eruption, New Zealand: Landscape responses to a large-scale explosive rhyolite eruption. *Sedimentary Geology 220, 319-336.*

Maurice S., Wiens R. C., Saccoccio M., Barraclough B., Gasnault O., Forni O., ... & Bernardin J. (2012). The ChemCam instrument suite on the Mars Science Laboratory (MSL) rover: science objectives and mast unit description. *Space science reviews, 170(1-4), 95-166.*

Maurice S., Cousin A., Wiens R., Gasnault O., Parès L., Forni O., Meslin P.Y., Clegg S., & ChemCam Team (2013). Laser Induced Breakdown Spectroscopy (LIBS) Spot Size at Stand-Off Distances with ChemCam. In *Lunar and Planetary Science Conference, Vol. 43, p. 1659.*

Maurice S., Clegg S., Wiens R. C., Gasnault O., Rapin W., Forni O., Cousin A., Sautter V., Mangold N., Le Deit L, et al. (2016). ChemCam activities and discoveries during the nominal mission of the Mars Science Laboratory in Gale Crater. *Mars. JAAS vol. 31, pp. 863-889. DOI: 10.1039/c5ja00417a*

McCubbin F. M., Barnes J. J., Santos A. R., Boyce J. W., Anand M., Franchi I. A., Agee C. B. (2016). Hydrogen Isotopic Composition of Apatite in Northwest Africa 7034: A Record of the "Intermediate" H-Isotopic Reservoir in the Martian Crust? In *Lunar and Planetary Science Conference, Vol 47, p.1326.*

McLennan S. M., Anderson R. B., Bell J. F., Bridges J. C., Calef F., Campbell J. L., ... & Des Marais D. J. (2014). Elemental geochemistry of sedimentary rocks at Yellowknife Bay, Gale crater, Mars. *Science, 343*(*6169), 1244734.*

McSween H. Y., Murchie S. L., Crisp J. A., Bridges N. T., Anderson R. C., Bell J. F., ... & Ghosh A. (1999). Chemical, multispectral, and textural constraints on the composition and origin of rocks at the Mars Pathfinder landing site. *Journal of Geophysical Research: Planets, 104(E4), 8679-8715.*

McSween H. Y., Grove T. L., Wyatt M. B. (2003). Constraints on the composition and petrogenesis of the Martian crust, *Journal of Geophysical Research, Volume 108, Issue E12, pp. 9-1. Doi:10.1029/2003JE002175*

McSween H. Y., Ruff S. W., Morris R. V., Bell J. F., Herkenhoff K., Gellert R., … Schmidt M. (2006a). Alkaline volcanic rocks from the Columbia Hills, Gusev crater, Mars. *Journal of Geophysical Research E: Planets, 111, 1–15. doi:10.1029/2006JE00269.*

McSween, H. Y., Wyatt, M. B., Gellert, R., Bell, I. F., Morris, R. V., Herkenhoff, K. E., … Zipfel, J. (2006b). Characterization and petrologic interpretation of olivine-rich basalts at Gusev Crater, Mars. *Journal of Geophysical Research E: Planets, 111(2), E02S10. doi:10.1029/2005JE002477*

McSween H. Y, Taylor G. J., Wyatt M. (2009) Elemental composition of the Martian crust, *Science, **324**, 736–739 doi: 10.1126/science.1165871*

Meslin, P. Y., Gasnault, O., Forni, O., Schröder, S., Cousin, A., Berger, G., ... & Le Mouélic, S. (2013). Soil diversity and hydration as observed by ChemCam at Gale Crater, Mars. *Science, 341(6153), 1238670.*

Meyer, C. (2015), The Mars Meteorite Compendium, astromaterials res. Andexplor. Sci. , Lyndon B. Johnson Space Cent., Houston, Tex. 5 [available at http://curator.jsc.nasa.gov/antme/mmc/index.cfm]

Mikouchi, T. (2001) Mineralogical similarities and differences between the Los Angeles basaltic shergottite and the Asuka-881757 lunar mare meteorite. *Antarct. Meteorites Res., 14, 1-20.*

Mikouchi T., Koizumi E., Monkawa A., Ueda Y., Miyamoto M. (2003). Mineralogy and petrology of Yamato 000593: Comparison with other Martian nakhlite meteorites. *Antartic Meteorite Research, Vol. 16, pp. 34-57.*

Morris, R.V., Vaniman D., Blake D., Gellert R., Chipera S., Rampe E., Ming D., et al. (2016) Silicic Volcanism on Mars evidenced by tridymite detection in high-SiO2 sedimenatary rock at Gale crater. *In press at Proceedings of the National Academy of Sciences*

Nyquist L. E., Shish C.-Y., McCubbin F. M., Santos A., R., Shearer C. K., Peng Z. X., Burger P. V., Agee C. B. (2016). Rb-Sr and Sm-Nd isotopic and REE studies of igneous components in the bulk matrix domain of Martian breccia Northwest Africa 7034. *Meteoritics & Planetary Science, Vol. 51, Issue 3, pp. 483-498.*

Ollila, A. M., Newsom, H. E., Clark, B., Wiens, R. C., Cousin, A., Blank, J. G., ... & Gasnault, O. (2014). Trace element geochemistry (Li, Ba, Sr, and Rb) using Curiosity's ChemCam: Early results for Gale crater from Bradbury Landing Site to Rocknest. *Journal of Geophysical Research: Planets, 119(1), 255-285.*

Palucis M. C., Dietrich W. E., Hayes A. G., Williams R. M., Gupta S., Mangold N., ... & Sumner D. Y. (2014). The origin and evolution of the Peace Vallis fan system that drains to the Curiosity landing area, Gale Crater, Mars. *Journal of Geophysical Research: Planets, 119*(4), *705-728.*

Payré V., Fabre C., Cousin A., Forni O., Gasnault O., Sautter V., Wiens R., Ollila A., .. et al., Trace elements in Gale Crater: calibration update and quantification using ChemCam data. *In prep.*

Payré V., Fabre C., Cousin A., Forni, O. Gasnault O., Rapin W., ... & Clegg S. (2016, March). Trace Elements in Gale Crater: Li, Sr, Rb, and Ba Abundances Using Chemcam Data. In *Lunar and Planetary Science Conference (Vol. 47, p. 1348).*

Rapin W., Meslin P.Y., Maurice S., Vaniman D., Nachon M., Mangold N., Schröder S., et al., Hydration state of calcium sulfates in Gale crater, Mars: identification of bassanite veins, *accepted to EPSL*.

Rubin A. E., Warren P. H., Greenwood J. P., Verish R. S., Leshin L. A., Hervig R. L., Clayton R. N., Mayeda T. K. (2000). Los Angeles: The most differentiated basaltic martian meteorite. *Geology, Vol. 28, p.1011*.

Santos A. R., Agee C. B., McCubbin F. M., Shearer C. K., Burger P. V., Tartèse R., Anand M. (2015). Petrology of igneous clasts in Northwest Africa 7034: Implications for the petrologic diversity of the martian crust. *Geochimica et Cosmochimica Acta, Vol. 157, p. 56-85.*

Sautter V., Toplis M. J., Lorand J. P., & Macri M. (2012). Melt inclusions in augite from the nakhlite meteorites: A reassessment of nakhlite parental melt and implications for petrogenesis. *Meteoritics & Planetary Science, 47(3), 330-344.*

Sautter V., Fabre C., Forni O., Toplis M. J., Cousin A., Ollila A. M., ... & Mangold N. (2014). Igneous mineralogy at Bradbury Rise: The first ChemCam campaign at Gale crater. *Journal of Geophysical Research: Planets*, *119*(1), 30-46. doi: *10.1002/2013JE004472.*

Sautter V., Toplis M. J., Wiens R. C., Cousin A., Fabre C., Gasnault O., ... & Bridges J. C. (2015). *In situ* evidence for continental crust on early Mars. *Nature Geoscience, 8(8), 605-609. DOI: 10.1038/ngeo2474*

Sautter V., Toplis M. J., Beck P., Mangold N., Wiens R., Pinet P., ... & Gasnault O. (2016). Magmatic complexity on early Mars as seen through a combination of orbital, in-situ and meteorite data. *Lithos, 254, 36-52. DOI: 10.1016/j.lithos.2016.02.023*

Schmidt M. E., Campbell J. L., Gellert R., Perrett G. M., Treiman A. H., Blaney D. L., ... & Grotzinger J. (2014). Geochemical diversity in first rocks examined by the Curiosity Rover in Gale Crater: Evidence for and significance of an alkali and volatile-rich igneous source. *Journal of Geophysical Research: Planets, 119(1), 64-81. DOI: 10.1002/2013JE004481*

Schröder S., Meslin P. Y., Gasnault O., Maurice S., Cousin A., Wiens R. C., ... & Nachon M. (2015). Hydrogen detection with ChemCam at Gale crater. *Icarus, 249, 43-61.*

Shafer J.T, Brandon A.D., Lapen T.J., Righter M., Beard B. and Peslier A.H. (2009). Lu-Hf age of Martian meteorites Larkman Nunatek 06319, In *Lunar and Planetary Science Conference (Vol. 40, p. 1803).*

Shirai N. and Ebihara M. (2004) Chemical characteristics of a Martian meteorite, Yamato 980459. *Antarctic Meteorite Research, 17, 55-67.*

Squyres, S.W., et al. (2006) Rocks of Columbia Hills, *J. Geophys. Res. 11, E02S11, doi:10.1029/2005JE002562.*

Stockstill K. R., McSween H. Y., & Bodnar R. J. (2005). Melt inclusions in augite of the Nakhla Martian meteorite: Evidence for basaltic parental melt. *Meteoritics & Planetary Science*, *40*(3), *377-396.*

Stolper E. M., Baker M. B., Newcombe M. E., Schmidt M. E., Treiman A. H., Cousin A., ... & Leshin L. (2013). The petrochemistry of Jake_M: A Martian mugearite. *science*, *341(6153), 1239463. DOI: 10.1126/science.1239463.*

Taylor S. R. and S. McLennan (2009), Planetary Crusts, Cambridge, 378pp.

Thomas N. H., Ehlmann B. L., Clegg S. M., Forni O., Schröder S., Anderson D. E., ... & Delapp D. M. (2016, March). Characterization of Hydrogen in Basaltic Materials with Laser-Induced Breakdown Spectroscopy (LIBS). In *Lunar and Planetary Science Conference (Vol. 47, p. 2494).*

Treiman A. H., & Goodrich C. A. (2001, March). A parent magma for the Nakhla martian meteorite: reconciliation of estimates from 1-bar experiments, magmatic inclusions in olivine, and magmatic inclusions in augite. In *Lunar and Planetary Science Conference (Vol. 32).*

Treiman A. H. (2005). The nakhlite meteorites: Augite-rich igneous rocks from Mars. *Chemie der Erde-Geochemistry*, *65*(3), *pp. 203-270.*

Treiman A. H., Bish D. L., Vaniman D. T., Chipera S. J., Blake D. F., Ming D. W., ... & Rampe E. B. (2016). Mineralogy, Provenance, and Diagenesis of a Potassic Basaltic Sandstone on Mars: CheMin X-ray Diffraction of the Windjana Sample (Kimberley Area, Gale Crater). *Journal of Geophysical Research, Vol. 121, pp. 75-106.*

Udry A., Balta B., McSween H. Y. (2014a). Exploring fractionation models for Martian magmas. *Journal of Geophysical Research, Vol. 119, pp. 1-18.*

Udry A., Lunning N. G., McSween H. Y., & Bodnar R. J. (2014b). Petrogenesis of a vitrophyre in the martian meteorite breccia NWA 7034. *Geochimica et Cosmochimica Acta, 141, 281-293.*

Udry A., Howarth G. H. (2016). Petrogenesis of the Enriched Shergottite Northwest Africa 7320: A New Martian Gabbroic Sample. In *Lunar and Planetary Science Conference (Vol. 37), p.1730.*

Vaniman D. T., Bish D. L., Ming D. W., Bristow T. F., Morris R. V., Blake D. F., ... & Rice M. (2014). Mineralogy of a mudstone at Yellowknife Bay, Gale crater, Mars. *Science*, *343*(*6169), 1243480.*

Warren P. H., Greenwood J. P., Rubin A. E. (2004). Los Angeles: A tale of two stones. *Meteoritics & Planetary Science, Vol. 39, p.137-156.*

Wiens R. C., Maurice S., Barraclough B., Saccoccio M., Barkley W. C., Bell III J. F., ... & Bouyé M. (2012). The ChemCam instrument suite on the Mars Science Laboratory (MSL) rover: Body unit and combined system tests. *Space Science Reviews, 170*(*1-4), 167-227.*

Wiens R. C., Maurice S., Lasue J., Forni O., Anderson R. B., Clegg S., ... & Deflores L. (2013). Pre-flight calibration and initial data processing for the ChemCam laser-induced breakdown spectroscopy instrument on the Mars Science Laboratory rover. *Spectrochimica Acta Part B: Atomic Spectroscopy, 82, 1-27.*

Wiens R. (2015a, December). Major-Element Compositional Diversity Observed by ChemCam Along the MSL Traverse: The First Three Years. In *2015 AGU Fall Meeting*.

Wiens R.C., Maurice S., and the ChemCam and MSL Science Teams (2015b) ChemCam: Chemostratigraphy by the first Mars microprobe. *Elements 11, pp. 33-38*.

Wray J. J., Hansen S. T., Dufek, J., Swayze, G. A., Murchie, S. L., Seelos, F. P., Skok, J. R., Irwin, R. P., Ghiorso, M. S. 2013. Prolonged magmatic activity on Mars inferred from the detection of felsic rocks. *Nature Geoscience, Volume 6, Issue 12, pp. 1013-1017. DOI: 10.1038/ngeo1994*

LIST OF FIGURES

Figure 1: Curiosity's traverse up to sol 800. All igneous rocks observed by ChemCam are noted in black. Yellow circles correspond to CheMin analyses.

Figure 2: MastCam and RMI images of the effusive rocks. Red circle on the MastCam image represents the location of the RMI mosaic.
A. Pisolet, group 1; B. Gunflint group 1; C. Harrison, group 2; D. Robin_Hood, group 2; E. Becraft, group 3; F. Stark, group 3. White phenocrysts are easily observed on the Harrison and Robin_Hood targets (Group 2), whereas a shiny aphanitic texture is observed on Pisolet (Group 1).

Figure 3: MastCam and RMI images of the intrusive rocks. Red circle on the MastCam image represents the location of the RMI mosaic.
A. Beacon, group 4; B. La Reine, group 4; C. Ross, group 5; D. Nita, group 5. White and dark equigranular grains are visible in Beacon (Group 4), as well as big white crystals in Nita (Group 5).

Figure 4: FeO vs SiO_2 and Al_2O_3 vs (Na_2O+K_2O) for one representative target for each group. Each color-coded point corresponds to one observation point, and therefore to 25 shots (first 5 shots being removed to avoid dust contamination). a/ Group 1 Watterson FeO vs SiO_2, b/ Watterson Al_2O_3 vs (Na_2O+K_2O); c/ Group 2 Harrison FeO vs SiO_2, d/ Harrison Al_2O_3 vs (Na_2O+K_2O); e/ Group 3 Chakonipau FeO vs SiO_2, f/Chakonipau Al_2O_3 vs (Na_2O+K_2O); g/ Group 4 Ashuanipi FeO vs SiO_2, h/Ashuanipi Al_2O_3 vs (Na_2O+K_2O); i/ Group 5 Sparkle FeO vs SiO_2, j/Sparkle Al_2O_3 vs (Na_2O+K_2O).

Figure 5: a/ Ternary diagram (Ab-An-Or) for rocks of Group 2 trachyandesites and of Group 4. Martian meteorite feldspars envelope is superimposed for comparison (from Santos et al., 2015, Meyer et al., 2015). Feldspars sampled in these rocks are mainly andesines. b/ Left: Close up of elongated light-toned minerals of Harrison (Group 2). Among the visible points of this close-up, only points #12 and #16 are included in the ternary diagram on the left, the other points are either sampling a darker phase, or show a chemistry not consistent with feldspars. Right: close up of La_Reine (group 4) - no points are clearly sampling a light-toned phase on this rock. c/ Ternary diagram (Ab-An-Or) for felsic rocks of Group 3 and quartz-Diorite (Group 5). Martian meteorite feldspars envelope is superimposed for comparison (from Santos et al., 2015, Mars Meteorite Compendium. Feldspars sampled in Group 3 are mainly anorthoclase with few sanidines whereas Group 5 feldspars correspond to andesines. d/Left: MAHLI image of Clinton (Group 5) – no LIBS observation point has been made on this light-toned mineral. Right: close-up of Becraft with visible light-toned microliths (Group 3). Point #5 has sampled one of them.

Figure 6: Boxplot distributions of Rb, Sr, and Ba predictions and of Cr peak area for all igneous groups. Cr is not quantified yet with the ChemCam instrument and therefore we are showing here peak areas only. The boxplot distribution gives access to three different information: 1/the median is given by the line that divides the box itself; 2/ 50% of the data fall into the box. The lower line of the box represents the lower quartile, and the upper line of the box represents the upper quartile; 3/ Each box is composed of "whiskers" that represent the data points that are outside the middle 50%. This figure shows that Group 3 rocks are significantly enriched in Ba and Rb (median is above the upper quartile of the other groups of rocks) consistent with the

presence of K-feldspars, whereas Group 1 is significantly enriched in Cr, due to more mafic phases.

Figure 7: Pyroxene quadrilateral where only points from dark-toned material are plotted, after chemical sorting. Martian meteorite pyroxene envelope is shown for comparison (From Udry et al., 2014b, Santos et al., 2015; Mikouchi et al., 2001; Mikouchi et al., 2003). Pyroxenes sampled in igneous rocks at Gale contain more iron than sedimentary rocks analyzed by CheMin, but are comparable to pyroxenes in meteorites such as Los Angeles and QUE 94201.

Figure 8: A/ TAS diagram modified from Sautter et al. (2015). The dashed black line is a calculated fractional crystallization trend of a primary liquid produced by 6% partial melting at a pressure of 1 GPa of an anhydrous primitive mantle composition (Sautter et al., 2015 in SOM §4); B/ MgO/FeO vs Al_2O_3/SiO_2, with MER APXS superimposed to Groups 1, 3, & 4. All the data presented in this figure are normalized to 100%. In this figure are reported only Groups 1 and 4 that are new compared to previous studies, as well as Meeting_House from Group 3.

Figure 9: Statistics (A) on igneous rocks (in %) and their distribution (B) along the traverse.

LIST OF TABLES

Table 1: Characteristics of the Curiosity's scientific cameras.

Table 2: List of all igneous rocks observed with ChemCam, based on textural analysis. Sol of acquisition as well as raster type are provided. Raster type gives the number of observation points performed on the target, as well as the grid shape. For example, a raster type of « 3x3 » corresponds to a grid of 3 observation points/row with 3 rows, « 1x5 » corresponds to a vertical transect of 5 observation points and in contrary « 5x1 » corresponds to a horizontal transect of the same number of observation points.

Table 3: Representative compositions of the cleanest feldspars for each group containing feldspar crystals. Calculations are made on the basis of 8 oxygen atoms.

Table 4: Representative targets with the cleanest pyroxene analyses for each group where a pyroxene has been sampled. Calculations are made on the basis of 6 oxygens, except for Ruker #6 (24 oxygen atoms).

Table 5: Representative target points of cleanest oxide crystals analyzed in each group of igneous rocks.

Table 6: Whole-rock composition (normed to 100%) of representative targets for each group, as well as whole-rock composition estimation for Nakhlite Liquid parent from [*1]Treiman and Goodrich (2001) and [*2]Stockstill et al. (2005).

Table 7: Textural and Chemical summary table for each group.

Appendix – list of MCAM and RMI shown in figures

Figure 2:
A. Pisolet target: MastCam 0332MR1346001000E1 and RMI CRM_426959815_CCAM01332;
B. Gunflint group 1. MastCam 0329ML__426528429EDR_S0070136MCAM01329 and RMI CRM_426697580_CCAM03329;
C. Harrison, group 2. MastCam 0512MR2012000000E1 and RMI CRM_443119527_CCAM02514;
D. Robin_Hood, group 2. MastCam 0364ML1481094000E1 and RMI CRM_429891264_CCAM02365;
E. Becraft, group 3. MastCam 0421MR1726000000E1 and RMI CRM_434870001_CCAM04421;
F. Stark, group 3. MastCam 0003ML0000095000E1 and RMI CRM_398825626_CCAM03015.

Figure 3:
A. Beacon, group 4. MastCam 0374ML1539004000E1 and RMI CRM_430865915_CCAM01376;
B. La Reine, group 4. MastCam 0346MR1405000000E1 and RMI; CRM_428202685_CCAM01346;
C. Ross, group 5. MastCam 0379MR1564000000E1 and RMI CRM_431133527_CCAM02379;
D. Nita, group 5. MastCam 0544MR00219100103037l3E01 and RMI CRM_445794952_CCAM01544.

Figure 5:
Harrison target CRM_443119527_CCAM02514
La_Reine target CRM_428202685_CCAM01346
Clinton target - 0512MH00016300002008 84R00
Becraft target CRM_434870001_CCAM04421.

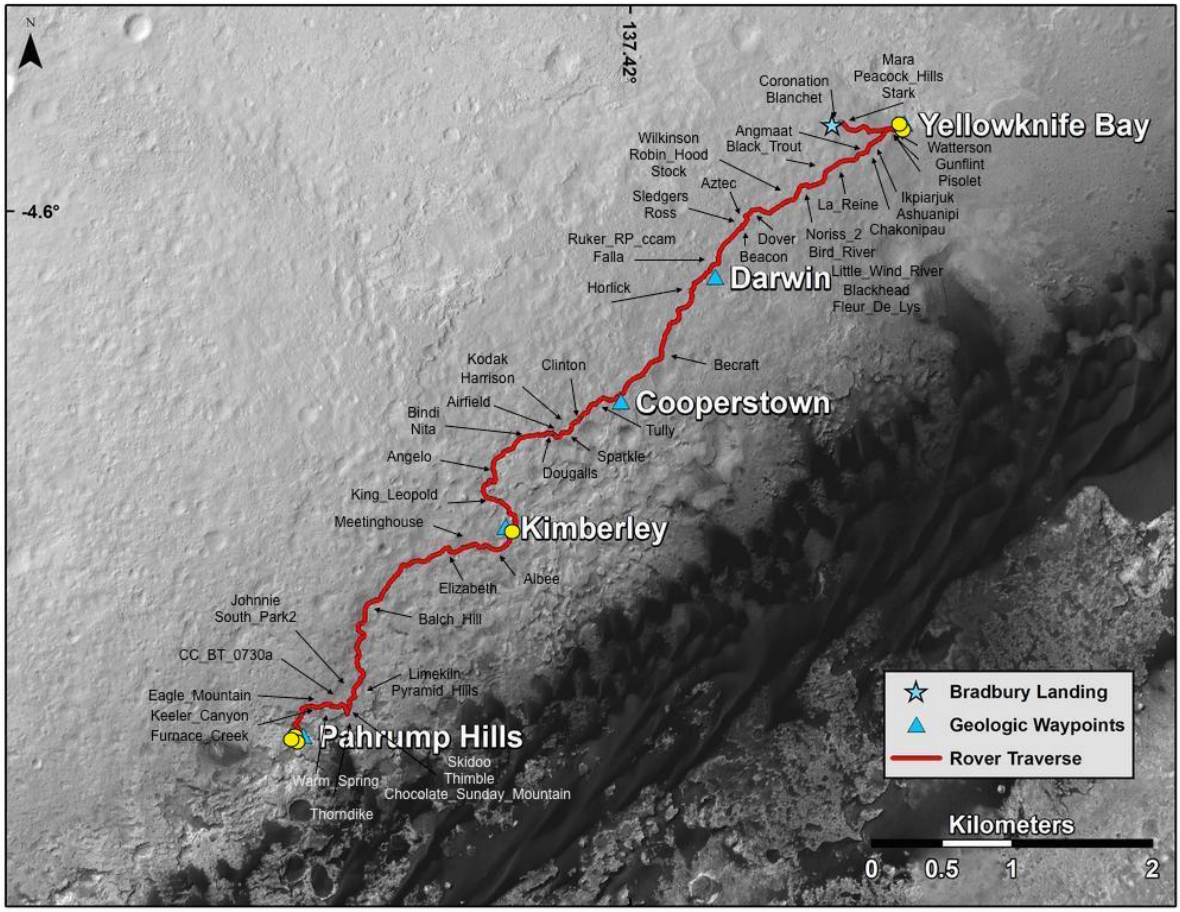

Figure 1.

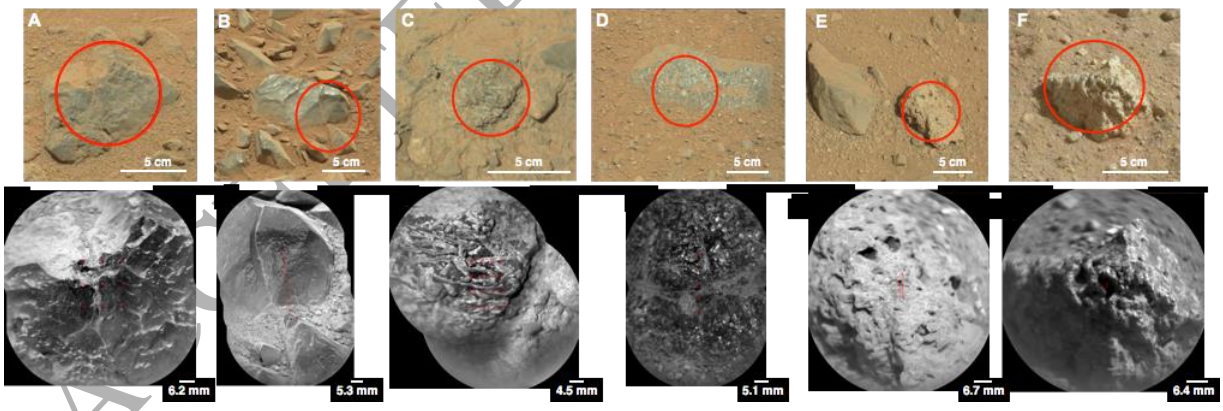

Figure 2

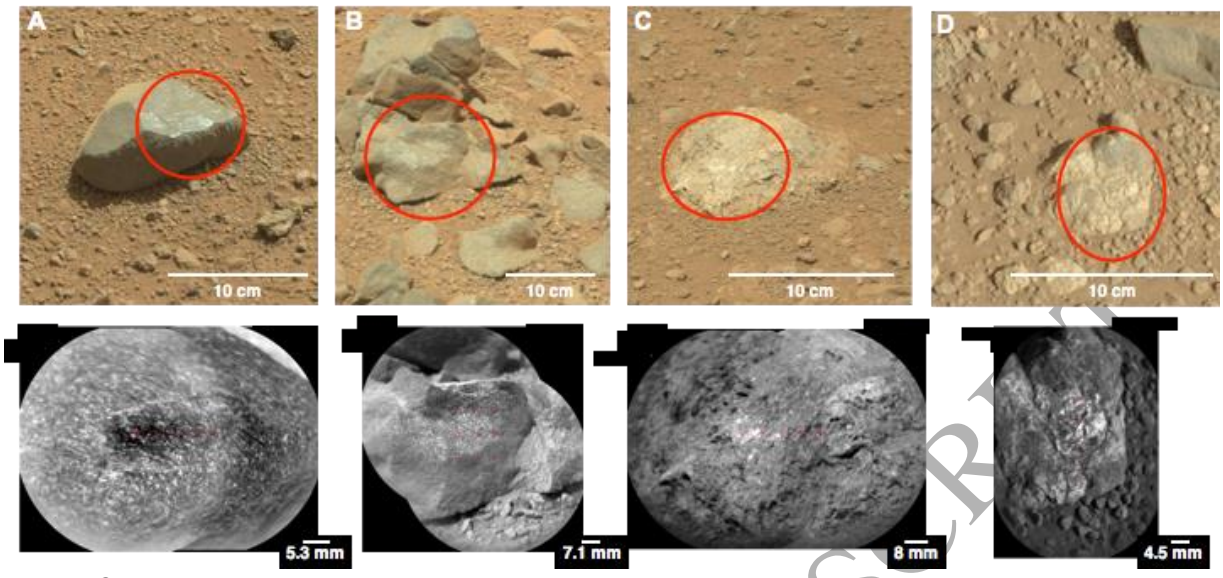

Figure 3

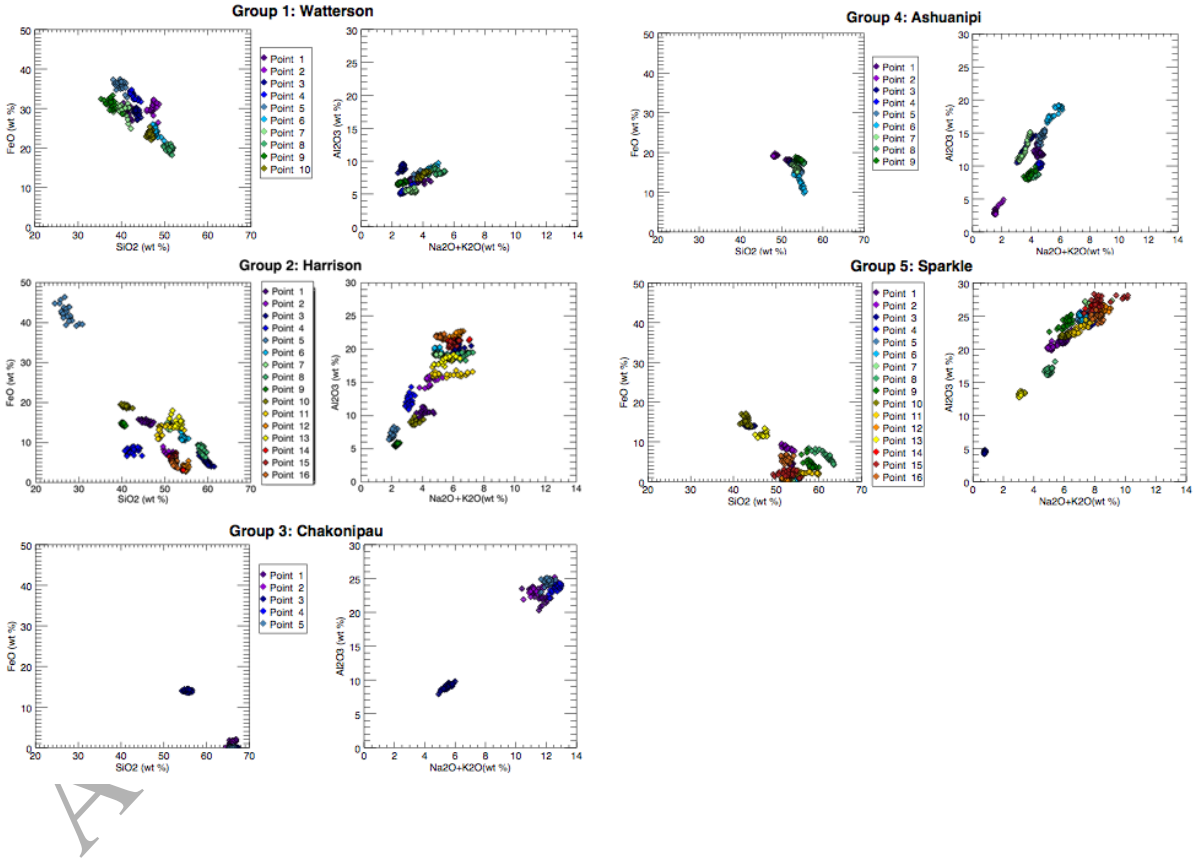

Figure 4

Figure5

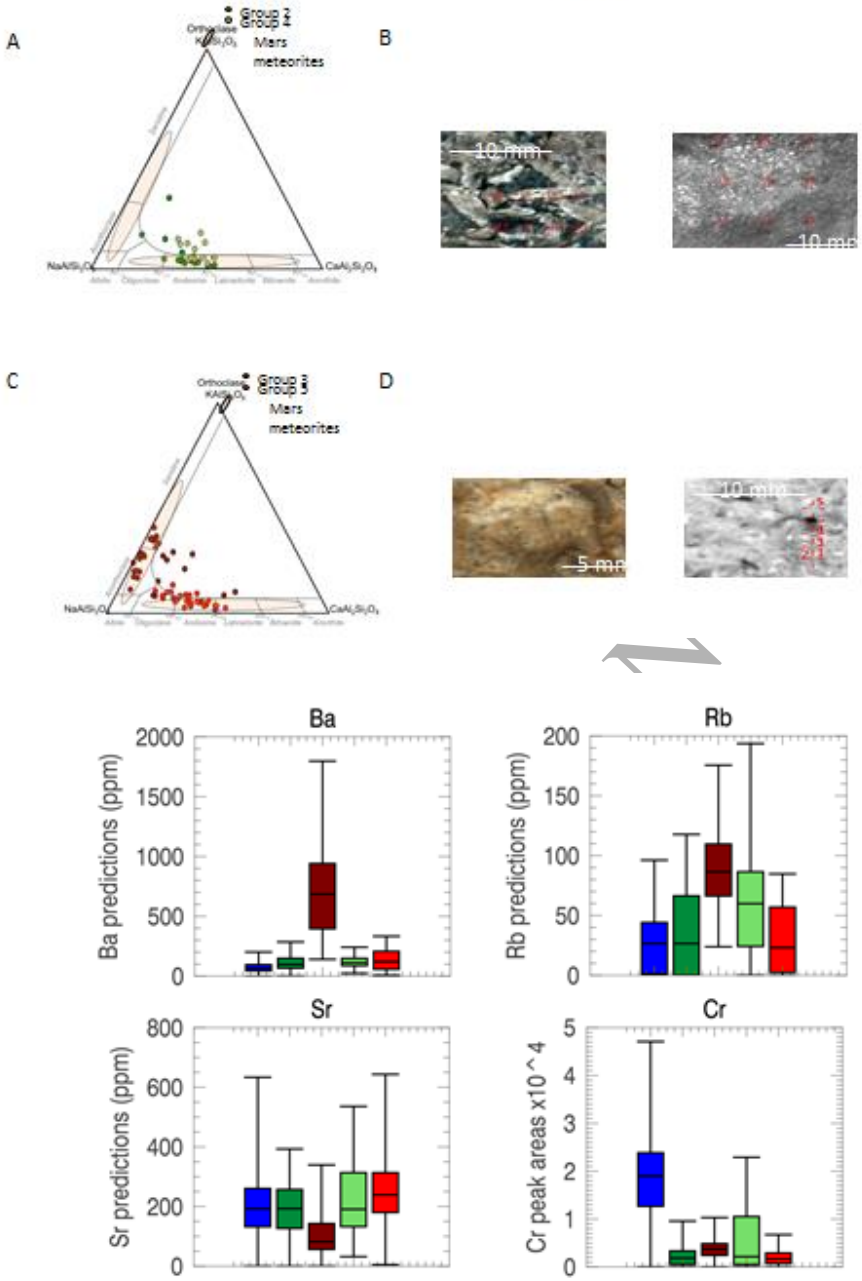

Figure 6

Figure 7

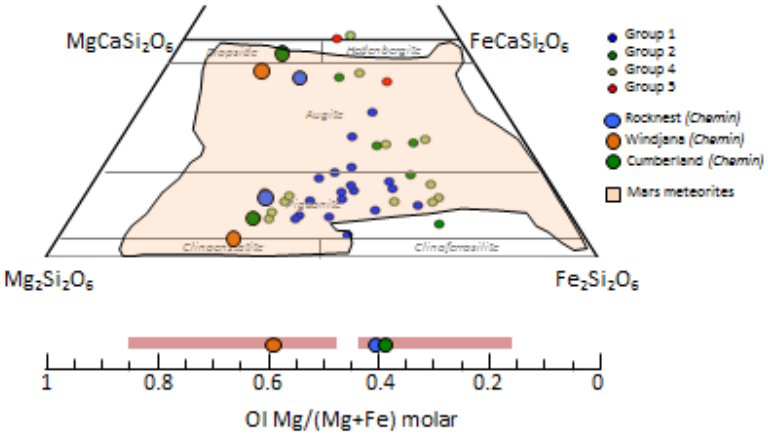

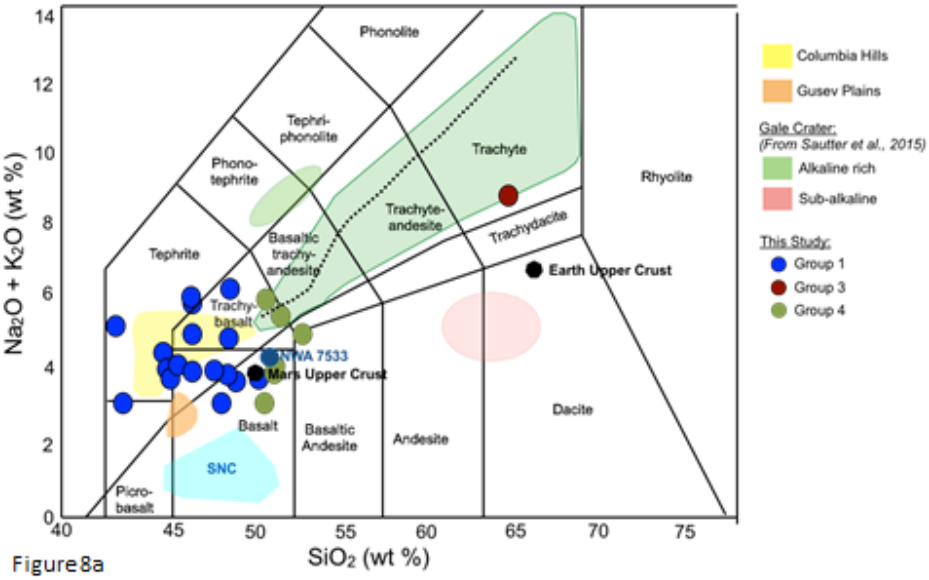

Figure 8a

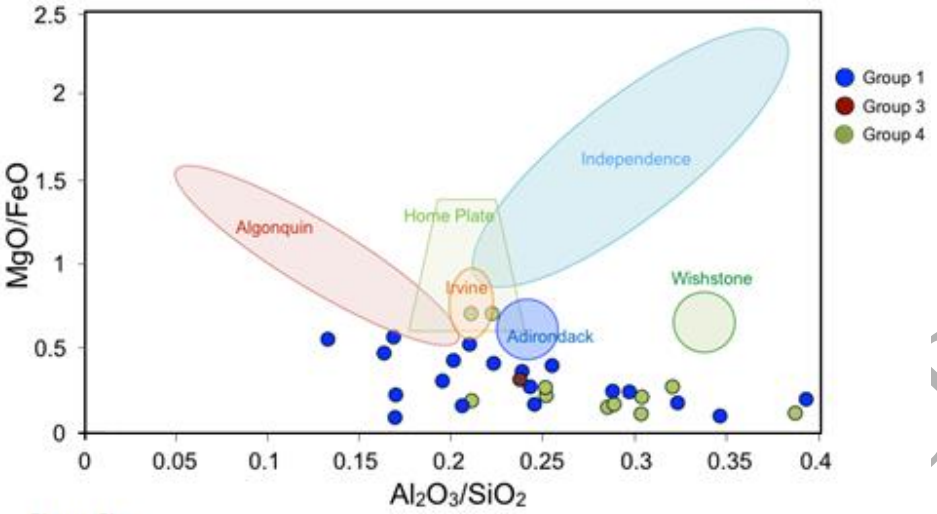

Figure 8b

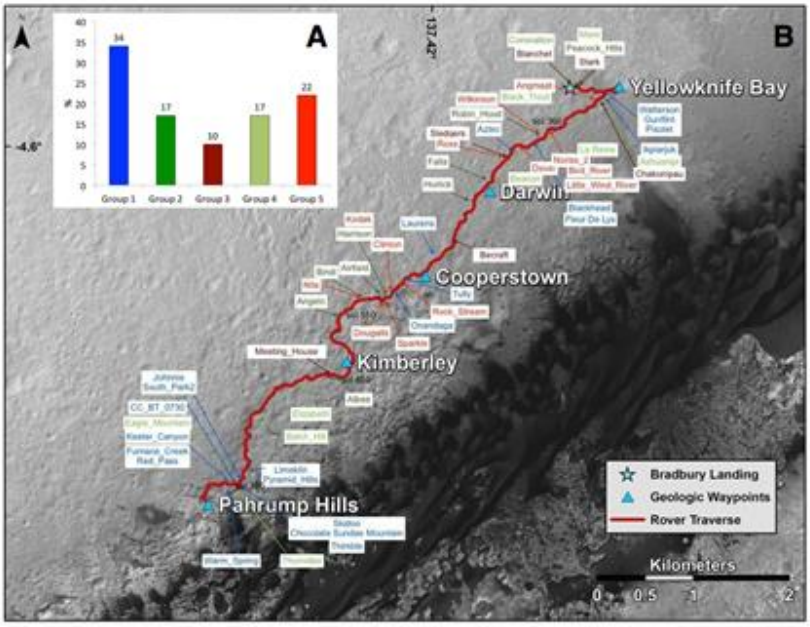

Figure 9

Table 1.

Camera	IFOV	Resolution	Focus range
MAHLI	34° to 38.4° (diagonal) or 402/346 microrad	Min 15μm/pix	2.1 cm to infinity
MastCam	M-100: 7.4×10^{-5} rad M-34: 2.2×10^{-4} rad	450μm/pix (left), 150 μm/pix (right)	2.1 m to infinity
RMI	20 mrad	19μrad/pix	1.2m to infinity

Table 2.

Group 1				Group 2				Group 3				Group 4				Group 5			
Aphanitic effusive dark-toned rocks				**Porphyritic effusive rocks**				**Aphanitic effusive light-toned rocks**				**Intrusive fine-grained rocks**				**Intrusive coarse-grained rocks**			
Name	Sol Number	Raster type	Gini Index	Name	Sol Number	Raster type	Gini Index	Name	Sol Number	Raster type	Gini Index	Name	Sol Number	Raster type	Gini Index	Name	Sol Number	Raster type	Gini Index
Watterson	329	1x10	0.5	Peacock_Hills	19	1x1	NA	Blanchet	13	1 image	NA	Coronation	13	1x1	NA	Noriss_2	356	3x3	0.74
Gunflint	329	1x10	0.42	Robin_Hood	365	1x5	NA	Stark	19	1x1	NA	Mara	19/20	1x1;1x5	NA	Dover	373	1x5	NA
Pisolet	332	3x3	0.61	Stock	368	3x3	0.65	Chakonipau	338	5x1	NA	Ashuanipi	337	3x3	0.64	Ross	379	5x1	NA
Ikpiarjuk	336	1x5	NA	Falla	390	3x3	0.81	Sledgers	379	3x3	0.67	La_Reine	346	3x3	0.6	Ruker_RP_ccam	387	3x3	0.81
Blackhead	367	3x3	0.76	Horlick	407	1x5	NA	Becraft	421	1x5	NA	Black_Trout	349	3x3	0.67	Clinton	511	5x1	NA
Fleur_de_Lys	370	1x5	NA	Harrison	512	4x4	0.79	Meetinghouse	653	1x5; 3x3	0.4	Beacon	376	6x1	NA	Sparkle	514	4x4	0.83
Aztec	377	1x5	NA	Airfield	523	1x5	NA					King_Leopold	574	3x3	0.72	Nita	544	1x5	NA
Tully	465	5x1	NA	Bindi	544	1x5	NA					Elizabeth	658	1x5	NA	*Altered rocks*			
Pyramid_Hills	692	1x5	NA	Albee	654	3x3	0.64					Eagle_Mountain	731	3x3	0.2	Angmaat	337	3x3	0.81
Johnnie	694	1x5	NA													Bird_River	358	1x5	NA
South_Park2	694	5x1	NA													Little_Wind_River	358	1 image	NA
Skidoo	700	10x1	0.46													Wilkinson	365	3x3	0.84
Chocolate_Sundae_Mountain	700	10x1	0.59													Kodak	512	5x1	NA
Thimble	704	5x1	NA													Dougalls	522	3x3	0.82
Thorndike	713	1x5	NA																
CC_BT_0730a	730	20x1	0																
Keeler_Canyon	732	5x1	NA																
Furnace_Creek	733	3x3	0.66																
Warm_Spring	739	3x3	0.71																

Table 3.

Group 1				Group 2				Group 3				Group 4				Group 5			
Aphanitic effusive dark-toned rocks				**Porphyritic effusive rocks**				**Aphanitic effusive light-toned rocks**				**Intrusive fine-grained rocks**				**Intrusive coarse-grained rocks**			
Name	Sol Number	Raster type	Gini Index	Name	Sol Number	Raster type	Gini Index	Name	Sol Number	Raster type	Gini Index	Name	Sol Number	Raster type	Gini Index	Name	Sol Number	Raster type	Gini Index
Watterson	329	1x10	0.5	Peacock_Hills	19	1x1	NA	Blanchet	13	1 image	NA	Coronation	13	1x1	NA	Noriss_2	356	3x3	0.74
Gunflint	329	1x10	0.42	Robin_Hood	365	1x5	NA	Stark	19	1x1	NA	Mara	19/20	1x1;1x5	NA	Dover	373	1x5	NA
Pisolet	332	3x3	0.61	Stock	368	3x3	0.65	Chakonipau	338	5x1	NA	Ashuanipi	337	3x3	0.64	Ross	379	5x1	NA
Ikpiarjuk	336	1x5	NA	Falla	390	3x3	0.81	Sledgers	379	3x3	0.67	La_Reine	346	3x3	0.6	Ruker_RP_ccam	387	3x3	0.81
Blackhead	367	3x3	0.76	Horlick	407	1x5	NA	Becraft	421	1x5	NA	Black_Trout	349	3x3	0.67	Clinton	511	5x1	NA
Fleur_de_Lys	370	1x5	NA	Harrison	512	4x4	0.79	Meetinghouse	653	1x5; 3x3	0.4	Beacon	376	6x1	NA	Sparkle	514	4x4	0.83
Aztec	377	1x5	NA	Airfield	523	1x5	NA					King_Leopold	574	3x3	0.72	Nita	544	1x5	NA
Tully	465	5x1	NA	Bindi	544	1x5	NA					Elizabeth	658	1x5	NA	*Altered rocks*			
Pyramid_Hills	692	1x5	NA	Albee	654	3x3	0.64					Eagle_Mountain	731	3x3	0.2	Angmaat	337	3x3	0.81
Johnnie	694	1x5	NA													Bird_River	358	1x5	NA
South_Park2	694	5x1	NA													Little_Wind_River	358	1 image	NA
Skidoo	700	10x1	0.46													Wilkinson	365	3x3	0.84
Chocolate_Sundae_Mountain	700	10x1	0.59													Kodak	512	5x1	NA
Thimble	704	5x1	NA													Dougalls	522	3x3	0.82
Thorndike	713	1x5	NA																
CC_BT_0730a	730	20x1	0																
Keeler_Canyon	732	5x1	NA																
Furnace_Creek	733	3x3	0.66																
Warm_Spring	739	3x3	0.71																

Table 4.

Group 1				Group 2				Group 3				Group 4				Group 5			
Aphanitic effusive dark-toned rocks				**Porphyritic effusive rocks**				**Aphanitic effusive light-toned rocks**				**Intrusive fine-grained rocks**				**Intrusive coarse-grained rocks**			
Name	Sol Number	Raster type	Gini Index	Name	Sol Number	Raster type	Gini Index	Name	Sol Number	Raster type	Gini Index	Name	Sol Number	Raster type	Gini Index	Name	Sol Number	Raster type	Gini Index
Watterson	329	1x10	0.5	Peacock_Hills	19	1x1	NA	Blanchet	13	1 image	NA	Coronation	13	1x1	NA	Noriss_2	356	3x3	0.74
Gunflint	329	1x10	0.42	Robin_Hood	365	1x5	NA	Stark	19	1x1	NA	Mara	19/20	1x1;1x5	NA	Dover	373	1x5	NA
Pisolet	332	3x3	0.61	Stock	368	3x3	0.65	Chakonipau	338	5x1	NA	Ashuanipi	337	3x3	0.64	Ross	379	5x1	NA
Ikpiarjuk	336	1x5	NA	Falla	390	3x3	0.81	Sledgers	379	3x3	0.67	La_Reine	346	3x3	0.6	Ruker_RP_ccam	387	3x3	0.81
Blackhead	367	3x3	0.76	Horlick	407	1x5	NA	Becraft	421	1x5	NA	Black_Trout	349	3x3	0.67	Clinton	511	5x1	NA
Fleur_de_Lys	370	1x5	NA	Harrison	512	4x4	0.79	Meetinghouse	653	1x5; 3x3	0.4	Beacon	376	6x1	NA	Sparkle	514	4x4	0.83
Aztec	377	1x5	NA	Airfield	523	1x5	NA					King_Leopold	574	3x3	0.72	Nita	544	1x5	NA
Tully	465	5x1	NA	Bindi	544	1x5	NA					Elizabeth	658	1x5	NA	*Altered rocks*			
Pyramid_Hills	692	1x5	NA	Albee	654	3x3	0.64					Eagle_Mountain	731	3x3	0.2	Angmaat	337	3x3	0.81
Johnnie	694	1x5	NA													Bird_River	358	1x5	NA
South_Park2	694	5x1	NA													Little_Wind_River	358	1 image	NA
Skidoo	700	10x1	0.46													Wilkinson	365	3x3	0.84
Chocolate_Sundae_Mountain	700	10x1	0.59													Kodak	512	5x1	NA
Thimble	704	5x1	NA													Dougalls	522	3x3	0.82
Thorndike	713	1x5	NA																
CC_BT_0730a	730	20x1	0																
Keeler_Canyon	732	5x1	NA																
Furnace_Creek	733	3x3	0.66																
Warm_Spring	739	3x3	0.71																

Table 5.

	Group 1	Group 2	Group 3	Group 4	Group 5
	Watterson #9	Horlick #4	Chakonipau #3	Beacon #6	Noriss_2 #6
SiO2	38.49	37.35	55.46	41.52	38.97
TiO2	1.42	3.80	13.05	2.47	2.81
Al2O3	6.68	6.98	9.02	6.61	4.69
FeO	31.73	28.77	14.11	19.21	20.44
MgO	2.58	2.69	2.89	3.45	3.58
CaO	6.07	4.25	4.12	7.34	9.22
Na2O	2.23	3.14	4.43	2.85	1.69
K2O	0.34	1.44	1.04	0.27	0.18
Sum	89.52	88.42	104.11	83.72	81.59

Table 6.

	Group 1	Group 2	Group 3	Group 4	Group 5
	Watterson #9	Horlick #4	Chakonipau #3	Beacon #6	Noriss_2 #6
SiO2	38.49	37.35	55.46	41.52	38.97
TiO2	1.42	3.80	13.05	2.47	2.81
Al2O3	6.68	6.98	9.02	6.61	4.69
FeO	31.73	28.77	14.11	19.21	20.44
MgO	2.58	2.69	2.89	3.45	3.58
CaO	6.07	4.25	4.12	7.34	9.22
Na2O	2.23	3.14	4.43	2.85	1.69
K2O	0.34	1.44	1.04	0.27	0.18
Sum	89.52	88.42	104.11	83.72	81.59

Table 7.

	Group #	# of rocks	Texture				Mineralogical phases			Rock type
			Shape	*Color*	*Grains size*	*Crystals*	*Mafic phases*	*Feldspars*	*Other*	
Effusive rocks	*Group 1*	20	- Conchoidal fractures - Glassy material	Dark & shiny	Aphanitic (<0.3 mm)	Most with light-toned microliths	- Pigeonites (Mg# = 0.2-0.65)	No clean analysis	- Fe/Ti oxides - F-bearing minerals	Basalt, basanite
	Group 2	10		Dark	Porphyritic (up to 2 cm long)	- Light-toned euhedral phenocrysts - Up to 80% of the rock	- Ferro-pigeonites - Few ferro-augites	- Andesines - Harrison with zonations: andesine core / K-feldspar rim	- Fe-Ti-Cr oxides - F-bearing minerals and possible apatite (Harrison #4)	Trachy-andesite
	Group 3	6	- Conchoidal fractures - Vesiculated or pumiceous	Leucocratic	Very fine-grained to aphanitic 0.3 -1 mm	None visible	No dark minerals visible	- Anorthoclases - Sanidines	- Fe/Ti oxides with possible Cl enrichments	Trachyte
Intrusive rocks	*Group 4*	10	- Rounded edge - Flat or curved facets	Grey	Fine to coarse grained (<3 mm)	- 1/2 dark + 1/2 light equigranular anhedral crystals	- Pigeonites (Mg# = 20-65%) - Few ferro-augites	Andesines	- Fe/Ti/Cr oxides - F-bearing minerals	Gabbro, Norite
	Group 5	13		Leucocratic	Coarse-grained (>5 mm)	- Light-toned anhedral: 80% of the rock - Rectangular translucent grey grains - Pinky coarse crystals - Secondary minerals	- Pigeonites (Mg# = 20-65%) - Few ferro-augites	- Andesines -Oligoclases	- Amphiboles? - Quartz intergrown with plagioclases - Fe/Ti oxides	Quartzodiorite Granodiorite